

# Geodesic Slice Sampling on the Sphere

Michael Habeck<sup>1</sup>

MICHAEL.HABECK@UNI-JENA.DE

Mareike Hasenpflug<sup>2</sup>

MAREIKE.HASENPFLUG@UNI-PASSAU.DE

Shantanu Kodgirwar<sup>1</sup>

SHANTANU.KODGIRWAR@UNI-JENA.DE

Daniel Rudolf<sup>2</sup>

DANIEL.RUDOLF@UNI-PASSAU.DE

<sup>1</sup>*Friedrich Schiller University Jena, 07743 Jena, Germany*

<sup>2</sup>*Universität Passau, Innstraße 33, 94032 Passau, Germany*

**Editor:** My editor

## Abstract

Probability measures on the sphere form an important class of statistical models and are used, for example, in modeling directional data or shapes. Due to their widespread use, but also as an algorithmic building block, efficient sampling of distributions on the sphere is highly desirable. We propose a shrinkage based and an idealized geodesic slice sampling Markov chain, designed to generate approximate samples from distributions on the sphere. In particular, the shrinkage-based version of the algorithm can be implemented such that it runs efficiently in any dimension and has no tuning parameters. We verify reversibility and prove that under weak regularity conditions geodesic slice sampling is uniformly ergodic. Numerical experiments show that the proposed slice samplers achieve excellent mixing on challenging targets including the Bingham distribution and mixtures of von Mises-Fisher distributions. In these settings our approach outperforms standard samplers such as random-walk Metropolis-Hastings and Hamiltonian Monte Carlo.

**Keywords:** Markov Chain Monte Carlo, slice sampling, spherical distributions

## 1 Introduction

In recent years, with the advent of sampling methods based on Markov chains, Bayesian inference with posterior distributions on manifolds attracted considerable attention. In particular, various Markov chain algorithms for approximate sampling on manifolds have been developed (see Byrne and Girolami, 2013; Lan et al., 2014; Goyal and Shetty, 2019; Lie et al., 2023; Beskos and Kamatani, 2022). Here we focus on the prototypical case of the sphere embedded in  $\mathbb{R}^d$  with its inherent geometrical features as the underlying manifold. Following the slice sampling paradigm, we introduce and analyze an efficient way of approximate sampling of distributions on the sphere.

Let  $\mathbb{S}^{d-1}$  be the  $(d-1)$ -dimensional Euclidean unit sphere in  $\mathbb{R}^d$  and let  $\sigma_{d-1}$  denote the volume measure on  $\mathbb{S}^{d-1}$ . For  $p: \mathbb{S}^{d-1} \rightarrow (0, \infty)$  satisfying

$$Z := \int_{\mathbb{S}^{d-1}} p(x) \sigma_{d-1}(dx) \in (0, \infty), \quad (1)$$

we are interested in a target distribution  $\pi$  of the form

$$\pi(dx) = \frac{1}{Z} p(x) \sigma_{d-1}(dx), \quad (2)$$

such that  $p/Z$  is the probability density function of  $\pi$  relative to  $\sigma_{d-1}$ . In a Bayesian setting,  $\pi$  can be considered a posterior distribution determined by likelihood  $p$  and prior measure  $\sigma_{d-1}$ . Throughout the paper, we assume that  $p$  can be evaluated, which is a common minimal requirement in the Markov chain Monte Carlo (MCMC) literature. Our motivation for considering MCMC on the sphere is twofold:

1. *Posteriors naturally defined on the sphere require efficient sampling:* Sampling distributions on the sphere play an important role in directional statistics and shape analysis (see Mardia and Jupp, 2000), and Bayesian inverse problems on  $\mathbb{S}^2$  occur, e.g., in astrophysics or geophysics (see Marignier et al., 2023). Moreover, Bayesian density estimation (Holbrook et al., 2020) requires sampling of a posterior on an infinite-dimensional sphere, which usually is approximated by truncating the dimension, ending up with  $\mathbb{S}^{d-1}$  for large  $d$ .
2. *Spherical sampling can be used as tool within transforming Markov chains:* Lan et al. (2014) introduced a Hamiltonian Monte Carlo (HMC) scheme for sampling from spherical distributions that leads, after suitable transformations, to an efficient exploration of distributions in  $\mathbb{R}^d$  constrained by inequalities. Recently, Yang et al. (2022) demonstrated that MCMC algorithms on  $\mathbb{S}^{d-1}$  can target distributions in  $\mathbb{R}^d$  by mapping them to the sphere by means of the stereographic projection. They report that for their proposed algorithms this approach is advantageous in heavy-tailed distribution scenarios.

We follow the slice sampling paradigm for approximately simulating  $\pi$ , since it allows us to avoid local random walk behavior, no tuning of a parameter such as a step-size is required and usually a richer choice of possible updates is offered, for details see Neal (2003); Murray et al. (2010). A transition mechanism for realizing a corresponding Markov chain works as follows: Given current state  $x \in \mathbb{S}^{d-1}$ , a superlevel set  $L(t)$  of  $p$  is randomly determined by choosing a level  $t \in (0, p(x))$ . Then, the next Markov chain instance is specified by (mimicking) sampling of the normalized reference measure  $\sigma_{d-1}$  restricted to the level set. The latter step requires some care regarding its algorithmic design. The main contributions of our paper are:

- We introduce an ideal geodesic slice sampler with corresponding Markov kernel  $H$  for approximately simulating  $\pi$ . The kernel  $H$  is implemented by moving along a randomly chosen great circle through the current state that forms a geodesic on  $\mathbb{S}^{d-1}$ . The resulting sampling on the geodesic intersected with the level set can be algorithmically realized by using an univariate acceptance/rejection approach.
- To increase the computational efficiency we propose a modification of  $H$  by employing a shrinkage procedure (cf. Murray et al. (2010) and Neal (2003)) and call the resulting Markov kernel  $\tilde{H}$ .
- We show that if  $p$  is lower semicontinuous, i.e., the strict superlevel sets of  $p$  are open, then both,  $H$  and  $\tilde{H}$  are well-defined and reversible with respect to (w.r.t.) the target distribution  $\pi$ .

- We prove uniform ergodicity for lower semicontinuous  $p$  that satisfy a boundedness condition, i.e., we provide total variation distance estimates of the  $n$ th marginal of a Markov chain with transition kernel  $H$  or  $\tilde{H}$  to  $\pi$ , see Theorem 6 and Theorem 16.
- We test our algorithms on challenging targets such as the Bingham distribution and mixtures of von Mises-Fisher distributions. We observe that our slice samplers outperform standard samplers such as random walk Metropolis Hastings (RWMH) and Hamiltonian Monte Carlo (HMC) on spherical distributions.

Let us comment on how our contributions fit into the literature. Lie et al. (2023) present two MCMC algorithms to sample distributions on the sphere using push forward kernels of a preconditioned Crank-Nicolson algorithm and of elliptical slice sampling, respectively. The crucial difference to our work is that Lie et al. (2023) assume that the target density is defined relative to an angular Gaussian distribution. Instead, here we consider target densities relative to the volume measure of the sphere. Observe that with increasing dimension both reference measures become “increasingly singular” to each other. Furthermore, Marignier et al. (2023) propose a proximal MCMC method to sample from posterior distributions of inverse imaging problems on  $\mathbb{S}^2$ . An infinite-dimensional setting of Bayesian density estimation is treated by Holbrook et al. (2020) by an HMC algorithm on a sphere. Other MCMC approaches have been developed on more general manifolds that usually cover  $\mathbb{S}^{d-1}$  as a special case. This includes the HMC algorithm for manifolds embedded in the Euclidean space introduced by Byrne and Girolami (2013) which uses the geodesic flow. Furthermore, Goyal and Shetty (2019) investigate a Metropolis-Hastings-like geodesic walk on manifolds with non-negative curvature. Here it is also worth to mention that several geodesic walks exist that target the uniform distribution on subsets of the sphere. We refer to Section 2.3 for more details. Finally, note that recently there has been some theoretical progress in the investigation of convergence properties of slice sampling (see for example Łatuszyński and Rudolf, 2024; Natarovskii et al., 2021b,a; Hasenpflug et al., 2024) that very much influenced the presentation and proof arguments of our theoretical results.

The outline of our paper is as follows: We start by introducing notation and details regarding the geometry of the sphere. In Section 3, we formulate the ideal and shrinkage slice sampler in terms of the transition kernel and transition mechanism. Here we also prove the reversibility and uniform ergodicity statements. Next we illustrate the applicability of our approach in different scenarios by numerical experiments. We conclude with a discussion.

## 2 Preliminaries

In this section we provide some general notation, give a brief introduction to geometrical features and explain how these can be leveraged to “walk the sphere”.

### 2.1 Setting and Notation

Let  $\lambda$  be the Lebesgue measure on  $\mathbb{R}$ , and let  $\|\cdot\|$  be the Euclidean norm induced by the standard inner product  $x^T y$ , where  $x, y \in \mathbb{R}^d$  for  $d \in \mathbb{N}$ . Moreover, define  $\text{Id}_d \in \mathbb{R}^{d \times d}$  to be the  $d$ -dimensional identity matrix. Throughout this paper we assume  $d \geq 3$  and consider the Euclidean unit sphere

$$\mathbb{S}^{d-1} := \{x \in \mathbb{R}^d \mid \|x\| = 1\}$$

equipped with its Borel- $\sigma$ -algebra  $\mathcal{B}(\mathbb{S}^{d-1})$ . By  $\sigma_{d-1}$  we denote the canonical volume measure on  $(\mathbb{S}^{d-1}, \mathcal{B}(\mathbb{S}^{d-1}))$  that serves as reference measure for distributions, cf. (2). To assess the difference of distributions  $\nu, \mu$  on  $(\mathbb{S}^{d-1}, \mathcal{B}(\mathbb{S}^{d-1}))$  we use the total variation distance

$$d_{tv}(\mu, \nu) := \sup_{A \in \mathcal{B}(\mathbb{S}^{d-1})} |\mu(A) - \nu(A)|.$$

On generic Borel space  $(\mathcal{X}, \mathcal{B}(\mathcal{X}))$  define the restriction of a measure  $\nu$  to a set  $A \in \mathcal{B}(\mathcal{X})$  by  $\nu|_A$ , that is  $\nu|_A(B) = \nu(A \cap B)$  for all  $B \in \mathcal{B}(\mathcal{X})$ . Whenever appropriate, for a set  $A \in \mathcal{B}(\mathcal{X})$  we denote by  $\mathcal{U}_A$  the uniform distribution on  $A$ . For example, for  $\mathcal{X} = \mathbb{R}$  with  $A \in \mathcal{B}(\mathbb{R})$  the probability measure  $\mathcal{U}_A$  refers to  $\frac{1}{\lambda(A)} \lambda|_A$  if  $\lambda(A) > 0$  and for  $\mathcal{X} = \mathbb{S}^{d-1}$  the distribution  $\mathcal{U}_{\mathbb{S}^{d-1}}$  refers to  $\frac{1}{\omega_{d-1}} \sigma_{d-1}$ , where  $\omega_{d-1} := \sigma_{d-1}(\mathbb{S}^{d-1})$ . Sometimes it is more convenient to work with random variables. Therefore, let  $(\Omega, \mathcal{F}, \mathbb{P})$  be a sufficiently rich probability space on which all random variables occurring in this paper are defined. If a random variable  $X$  has distribution  $\nu$ , we write  $X \sim \nu$ .

## 2.2 The Geometry of the Sphere

To approximately sample from distributions on the sphere we rely on its (special) geometry. The key objects in this context are great circles and “equators”. More formally regarding the latter, for given  $x \in \mathbb{S}^{d-1}$  we call

$$\mathbb{S}_x^{d-2} := \{v \in \mathbb{S}^{d-1} \mid v^T x = 0\}$$

the great subsphere with pole  $x$ . This  $(d-2)$ -dimensional subsphere is the intersection of  $\mathbb{S}^{d-1}$  and the  $(d-1)$ -dimensional hyperplane perpendicular to  $x$ , and in this sense can be thought of as a generalization of the equator. We also equip  $\mathbb{S}_x^{d-2}$  with the corresponding volume measure, which we denote as  $\mu_x$ . Since  $\mathbb{S}_x^{d-2}$  is essentially “a tilted  $\mathbb{S}^{d-2}$ ”, we have  $\mu_x(\mathbb{S}_x^{d-2}) = \omega_{d-2}$  for all  $x \in \mathbb{S}^{d-1}$ , cf. Appendix A. Accordingly  $\frac{1}{\omega_{d-2}} \mu_x$  coincides with  $\mathcal{U}_{\mathbb{S}_x^{d-2}}$ . In our transition mechanism, sampling w.r.t. the latter distribution frequently appears, such that we provide a procedure for performing it in Appendix A.

The great circles of the sphere are the “largest” 1-dimensional subspheres spanning  $\mathbb{S}^{d-1}$ . Rigorously, for every pair  $(x, v)$ , where  $x \in \mathbb{S}^{d-1}$  and  $v \in \mathbb{S}_x^{d-2}$ , we define the great circle

$$\gamma_{(x,v)} : \mathbb{R} \rightarrow \mathbb{S}^{d-1}, \quad \theta \mapsto \cos(\theta)x + \sin(\theta)v.$$

Intuitively, we can also think of  $\gamma_{(x,v)}$  as the curve obtained by “moving from the point  $x$  in the direction of  $v$  with a constant velocity”. This interpretation originates from Riemannian geometry and following their terminology we use the names great circle and geodesic interchangeably for the object  $\gamma_{(x,v)}$ . Note that all great circles passing through a point  $x \in \mathbb{S}^{d-1}$  are of the form  $\gamma_{(x,v)}$  for some  $v \in \mathbb{S}_x^{d-2}$ , i.e., the geodesics through  $x \in \mathbb{S}^{d-1}$  are parametrized by  $\mathbb{S}_x^{d-2}$ .

Observe, due to the periodicity of sine and cosine, that all great circles are  $2\pi$ -periodic. This is exploited when we incorporate the geodesics into our slice sampling approach.

We continue by illuminating an interaction between geometric and measure theoretic structure of the sphere with the help of the map

$$T_\theta : \mathbb{S}\mathbb{S}^{d-1} \rightarrow \mathbb{S}\mathbb{S}^{d-1}, \quad (x, v) \mapsto (\cos(\theta)x + \sin(\theta)v, \sin(\theta)x - \cos(\theta)v)$$

for  $\theta \in \mathbb{R}$ , where for brevity we define  $\mathcal{SS}^{d-1} := \bigcup_{x \in \mathbb{S}^{d-1}} (\{x\} \times \mathbb{S}_x^{d-2})$ . If we interpret for a pair  $(x, v) \in \mathcal{SS}^{d-1}$  the first component as position on the sphere and the second component as “direction of view”, then applying the map  $T_\theta$  to  $(x, v)$  can be thought of as “following the geodesic  $\gamma_{(x,v)}$  from  $x$  in direction  $v$  for a length of  $\theta$  and then doing a U-turn back on the spot”. This intuition is underpinned by the following lemma, proven in Appendix B, which essentially tells us that following the geodesic corresponding to the pair  $T_\theta(x, v)$  is the same as following the original geodesic  $\gamma_{(x,v)}$  in reverse direction with an offset of  $\theta$ .

**Lemma 1** *Let  $x \in \mathbb{S}^{d-1}$ ,  $v \in \mathbb{S}_x^{d-2}$ . For all  $\theta, r \in \mathbb{R}$  we have  $\gamma_{(x,v)}(\theta - r) = \gamma_{T_\theta(x,v)}(r)$ . In particular, this implies  $\gamma_{T_\theta(x,v)}(\theta) = x$ .*

Moreover, central to our proof techniques is the observation that the measure on  $\mathcal{SS}^{d-1}$  that “zips up” the volume measures  $\mu_x$  on the single fibers of  $\mathcal{SS}^{d-1}$  through the volume measure  $\sigma_{d-1}$  on  $\mathbb{S}^{d-1}$  is invariant under  $T_\theta$ .

**Lemma 2** *Let  $F : \mathcal{SS}^{d-1} \rightarrow \mathbb{R}$  be a function such that the left-hand side of the equation below exists. Then, for all  $\theta \in \mathbb{R}$  we have*

$$\int_{\mathbb{S}^{d-1}} \int_{\mathbb{S}_x^{d-2}} F(x, v) \mu_x(dv) \sigma_{d-1}(dx) = \int_{\mathbb{S}^{d-1}} \int_{\mathbb{S}_x^{d-2}} F(T_\theta(x, v)) \mu_x(dv) \sigma_{d-1}(dx). \quad (3)$$

For the convenience of the reader we provide the proof of the former lemma in Appendix B. For identity (3) in a setting of more general manifolds we refer to (Goyal and Shetty, 2019, Proof of Theorem 27).

### 2.3 Geodesic Walk on the Sphere.

Based on great circles we may “walk the sphere” starting at some state  $x \in \mathbb{S}^{d-1}$  by iteratively performing the following:

1. Choose a great circle  $\gamma$  through the given point  $x$  randomly.
2. Choose the next point on the great circle  $\gamma$  randomly.

For the first step in the outlined transition we can use the fact that geodesics through  $x \in \mathbb{S}^{d-1}$  are parametrized by  $\mathbb{S}_x^{d-2}$ . Namely, we realize “a random geodesic” as  $\gamma_{(x,v)}$ , where  $v$  is a sample from  $\mathcal{U}_{\mathbb{S}_x^{d-2}}$ , see Algorithm 5 in Appendix A for the simulation of this probability measure. The distribution of the randomly chosen point on the geodesic in step 2 significantly influences the stationary distribution of the random walk on the sphere. In this section, we consider it to be independent of  $x$ , which causes the stationary distribution to be the uniform one. In Section 3, we explain how the second step can be modified so as to obtain a Markov chain with a desired stationary probability measure.

Using a distribution  $\tau$  on  $[0, 2\pi)$  to sample on the geodesic, we obtain the following Markov kernel

$$K_\tau(x, A) := \int_{\mathbb{S}_x^{d-2}} \int_{[0, 2\pi)} \mathbb{1}_A(\gamma_{(x,v)}(\theta)) \tau(d\theta) \mathcal{U}_{\mathbb{S}_x^{d-2}}(dv)$$

with  $x \in \mathbb{S}^{d-1}, A \in \mathcal{B}(\mathbb{S}^{d-1})$ . The corresponding transition mechanism is described in Algorithm 1, where  $\tau$  can be interpreted as the distribution of the step-size.

---

**Algorithm 1** Geodesic random walk on the sphere.

---

**input:** current state  $x \in \mathbb{S}^{d-1}$

**output:** next state  $x'$

- 1: Draw  $V \sim \mathcal{U}_{\mathbb{S}_x^{d-2}}$ , call the result  $v$ .      {Perform Algorithm 5 with input  $x$ .}
  - 2: Draw  $\Theta \sim \tau$ , call the result  $\theta$ .
  - 3: Set  $x' = \cos(\theta)x + \sin(\theta)v$ .
- 

By Lemma 2 and Lemma 1 we have for any  $A, B \in \mathcal{B}(\mathbb{S}^{d-1})$  that

$$\begin{aligned} \int_B K_\tau(x, A) \sigma_{d-1}(dx) &= \int_{[0, 2\pi)} \int_{\mathbb{S}^{d-1}} \int_{\mathbb{S}_x^{d-2}} \mathbb{1}_B(x) \mathbb{1}_A(\gamma_{(x,v)}(\theta)) \frac{\mu_x(dv)}{\omega_{d-2}} \sigma_{d-1}(dx) \tau(d\theta) \\ &= \int_{[0, 2\pi)} \int_{\mathbb{S}^{d-1}} \int_{\mathbb{S}_x^{d-2}} \mathbb{1}_B(\gamma_{(x,v)}(\theta)) \mathbb{1}_A(x) \frac{\mu_x(dv)}{\omega_{d-2}} \sigma_{d-1}(dx) \tau(d\theta) = \int_A K_\tau(x, B) \sigma_{d-1}(dx), \end{aligned}$$

which yields that  $K_\tau$  is reversible w.r.t.  $\mathcal{U}_{\mathbb{S}^{d-1}}$ , see also Lee and Vempala (2018) or Goyal and Shetty (2019, Theorem 27).

Note that, depending on how  $\tau$  is chosen,  $K_\tau$  coincides with different random walks that have been discussed in the literature. We add some remarks related to this point:

**Related work.** If the step-size is chosen to be constant, that is,  $\tau = \delta_\varepsilon$  for  $\delta_\varepsilon$  being the Dirac measure on  $\mathbb{R}$  at  $\varepsilon \in (0, 2\pi)$ , then  $K_{\delta_\varepsilon}$  coincides with the geodesic walk from Mangoubi and Smith (2018) on the sphere. They provide dimension independent mixing time results for this walk on manifolds with bounded positive sectional curvature.

For targeting the uniform distribution on the sphere, the geodesic random walk introduced by Goyal and Shetty (2019, Algorithm 1, for their  $K = \mathbb{S}^{d-1}$ ) corresponds to  $K_\tau$  with  $\tau$  being the distribution of  $\varepsilon R$ , where  $R$  is a chi-distributed random variable with  $d-1$  degrees of freedom and fixed  $\varepsilon > 0$ . For manifolds with non-negative sectional curvature and bounded Riemannian curvature tensor, Goyal and Shetty (2019) provide mixing time results if their unfiltered walk is modified to target the uniform distribution of a strongly convex subset of the ambient manifold.

Moreover, the kernel  $K_{\delta_\varepsilon}$  is related to the retraction-based random walk introduced by Schwarz et al. (2022), where the geodesics are replaced by retractions, i.e., second order approximations of the geodesics. Schwarz et al. (2022) show that for  $\varepsilon \rightarrow 0$  this algorithm can be used to sample paths of the Brownian motion on a general manifold. Note, however, that this causes the stationary distribution of the resulting Markov chain to deviate from the uniform distribution.

General transitions according to  $K_\tau$  can also be interpreted as the repeated action of random rotations. The  $d$ -dimensional rotation matrix

$$G(y, z, \theta) = \text{Id}_d + (\cos(\theta) - 1)(yy^T + zz^T) + \sin(\theta)(yz^T - zy^T) \quad (4)$$

is the Givens rotation acting in the plane spanned by two orthogonal directions  $y, z \in \mathbb{S}^{d-1}$  where  $\theta$  is the rotation angle (see Givens, 1958). In this view, a transition of  $K_\tau$  to the next state  $X'$  is achieved by drawing an axis  $V \sim \mathcal{U}_{\mathbb{S}_x^{d-2}}$  and an angle  $\Theta \sim \tau$  to form a random Givens rotation that is applied to the current state  $x$ , i.e.,  $X' = G(V, x, \Theta)x$ .

A suitable reformulation of the latter can be viewed as a generalization of Kac’s random walk on the sphere (see e.g., Kac, 1956; Pillai and Smith, 2017). To perform a transition of Kac’s walk, draw  $1 \leq I < J \leq d$  and  $\Theta \sim \mathcal{U}_{(0,2\pi)}$  randomly to generate the next state  $X'$  by rotating the current state  $x$ , i.e.,  $X' = G(e_I, e_J, \Theta)x$ , where  $\{e_i\}_{i=1}^d$  is the standard basis of  $\mathbb{R}^d$ . Kac’s walk also approximately simulates the uniform distribution, but chooses the plane of rotation from a discrete set, whereas in the generalized version the plane of rotation changes continuously and always contains the current state  $x$ . Pillai and Smith (2017) show optimal mixing time results for Kac’s walk.

### 3 Geodesic Slice Sampling in $\mathbb{S}^{d-1}$

Following the slice sampling paradigm, we construct Markov chains for approximate sampling of  $\pi$  that rely on exploring the sphere along suitable 1-dimensional objects, the great circles. For this purpose let

$$L(t) := \{x \in \mathbb{S}^{d-1} \mid p(x) > t\}, \quad t \in (0, \infty),$$

be the superlevel set of  $p$ . Recall that  $p$  specifies  $\pi$ , cf. (2).

The rough idea is to choose a great circle  $\gamma_{(x,v)}$  and a level  $t$  randomly and then, from the intersection of the corresponding superlevel set and the great circle, draw the next state suitably. For  $x \in \mathbb{S}^{d-1}$ ,  $v \in \mathbb{S}_x^{d-2}$  and  $t \in (0, \infty)$  we require

$$L(x, v, t) := \{\theta \in [0, 2\pi) \mid p(\gamma_{(x,v)}(\theta)) > t\},$$

called geodesic level set, which contains all points on the great circle  $\gamma_{(x,v)}$  with the function value of  $p$  being greater than  $t$ . Naturally, this implies that level sets and geodesic level sets are linked via the identity

$$\mathbb{1}_{L(t)}(\gamma_{(x,v)}(\theta)) = \mathbb{1}_{L(x,v,t)}(\theta). \tag{5}$$

Exploiting lower semicontinuity of  $p$  we are able to identify a regime, where the geodesic level sets have strictly positive Lebesgue measure.

**Lemma 3** *For  $p$  being lower semicontinuous, any  $x \in \mathbb{S}^{d-1}$ ,  $t \in (0, p(x))$  and  $v \in \mathbb{S}_x^{d-2}$  we have  $\lambda(L(x, v, t)) > 0$ . Moreover, the essential supremum norm  $\|p\|_\infty$  of  $p$  w.r.t.  $\sigma_{d-1}$  coincides with  $\sup_{x \in \mathbb{S}^{d-1}} p(x)$ .*

**Proof** By the lower semicontinuity  $p^{-1}((t, \infty)) = L(t)$  is open, and by the fact that  $x \in L(t)$  it is also non-empty. Moreover, since  $\gamma_{(x,v)}$  is continuous we have that  $L(x, v, t) = \gamma_{(x,v)}^{-1}(L(t))$  is again open and non-empty, such that  $\lambda(L(x, v, t)) > 0$ . The final assertion follows by observing that  $L(\|p\|_\infty)$  is open (by the lower semicontinuity) and by the definition of  $\|p\|_\infty$  satisfies  $\sigma_{d-1}(L(\|p\|_\infty)) = 0$ . Consequently, we have  $L(\|p\|_\infty) = \emptyset$ , such that  $\|p\|_\infty = \sup_{x \in \mathbb{S}^{d-1}} p(x)$ . ■

In the following we always assume that  $p$  is lower semicontinuous, which implies by the previous lemma the well-definedness of the slice sampling schemes that we introduce now.

### 3.1 Ideal Geodesic Slice Sampling

We start by presenting an acceptance/rejection sampling based version of the geodesic slice sampler. For  $x \in \mathbb{S}^{d-1}$ ,  $t \in (0, p(x))$  and  $A \in \mathcal{B}(\mathbb{S}^{d-1})$  let

$$\begin{aligned} H_t(x, A) &:= \int_{\mathbb{S}_x^{d-2}} \int_{L(x,v,t)} \mathbb{1}_A(\gamma_{(x,v)}(\theta)) \frac{d\theta}{\lambda(L(x,v,t))} \frac{\mu_x(dv)}{\omega_{d-2}} \\ &= \int_{\mathbb{S}_x^{d-2}} \int_{L(x,v,t)} \mathbb{1}_A(\gamma_{(x,v)}(\theta)) \mathcal{U}_{L(x,v,t)}(d\theta) \mathcal{U}_{\mathbb{S}_x^{d-2}}(dv). \end{aligned}$$

The kernel  $H_t(x, \cdot)$  can be simulated by first choosing a random great circle  $\gamma_{(x,v)}$ , and then, by sampling a point from the uniform distribution on  $L(x, v, t)$ , the intersection of the great circle and the level set  $L(t)$ . The *ideal geodesic slice sampler* is given by the algorithm that implements a transition corresponding to the Markov kernel

$$H(x, A) := \frac{1}{p(x)} \int_0^{p(x)} H_t(x, A) dt = \int_0^{p(x)} H_t(x, A) \mathcal{U}_{(0,p(x))}(dt), \quad (6)$$

where  $x \in \mathbb{S}^{d-1}$ ,  $A \in \mathcal{B}(\mathbb{S}^{d-1})$ . In words, a level  $t \in (0, p(x))$  is chosen uniformly distributed before  $H_t(x, \cdot)$  is performed. A single transition of  $H$  is described in Algorithm 2 and a graphical illustration on  $\mathbb{S}^2$  is provided in Figure 1.

---

**Algorithm 2** Ideal geodesic slice sampler.

---

**input:** current state  $x \in \mathbb{S}^{d-1}$

**output:** next state  $x'$

- 1: Draw  $V \sim \mathcal{U}_{\mathbb{S}_x^{d-2}}$ , call the result  $v$ .      {Perform Algorithm 5 with input  $x$ .}
  - 2: Draw  $T \sim \mathcal{U}_{(0,p(x))}$ , call the result  $t$ .
  - 3: **repeat**
  - 4:    Draw  $\Theta \sim \mathcal{U}_{(0,2\pi)}$ , call the result  $\theta$ .
  - 5:    Set  $x' = \cos(\theta)x + \sin(\theta)v$ .
  - 6: **until**  $p(x') > t$ .
- 

**Remark 4** *The geodesic slice sampler can be viewed as an instance of the procedure described in Section 2.3 where the second step uses a distribution on the geodesic that depends on the initial point  $x$  and the chosen geodesic  $\gamma$ .*

We establish the correctness of the ideal geodesic slice sampler by arguing for reversibility w.r.t.  $\pi$  and by proving a quantitative convergence guarantee. The proof of the following result is provided in Appendix C.

**Proposition 5** *For  $\pi$  defined as in (2) with lower semicontinuous  $p$ , the kernel  $H$  is reversible w.r.t.  $\pi$ .*

Now we present our main result for the ideal geodesic slice sampler: Imposing a boundedness assumption on  $p$ , we provide an explicit convergence rate for the convergence to the stationary distribution in the total variation distance.



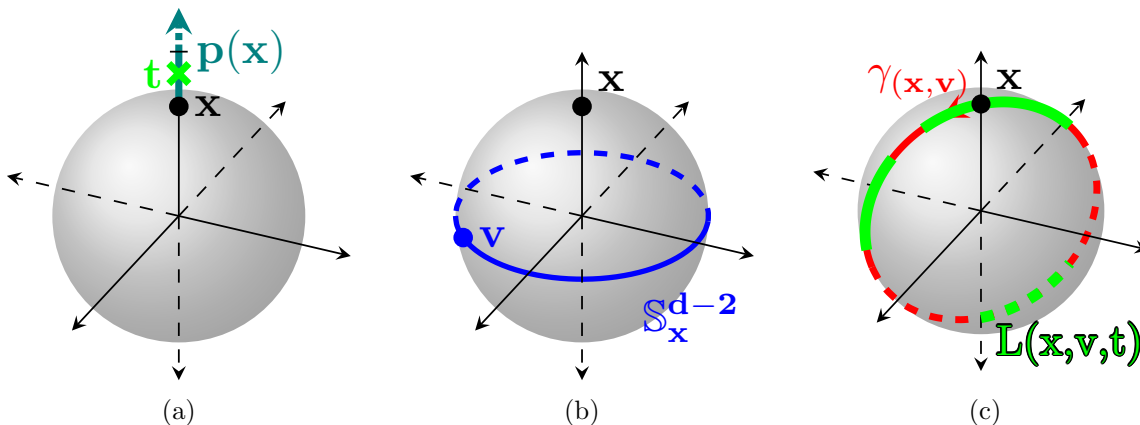


Figure 1: Transition mechanism of the ideal geodesic slice sampler. (a) Sample a random level  $t$  at the current point  $x$ . (b) Sample a random point  $v$  on  $\mathbb{S}_x^{d-2}$ . (c) Sample uniformly from the geodesic level set  $L(x, v, t)$ .

**Theorem 6** For  $p$  being lower semicontinuous with  $\|p\|_\infty < \infty$  we have

$$\sup_{x \in \mathbb{S}^{d-1}} d_{tv}(H^n(x, \cdot), \pi) \leq \left( 1 - \frac{\sup_{t>0} [t \cdot \mathcal{U}_{\mathbb{S}^{d-1}}(L(t))]}{\sqrt{2\pi}\sqrt{d-1} \|p\|_\infty} \right)^n, \quad \forall n \in \mathbb{N}, \quad (7)$$

where  $\sup_{t>0} [t \cdot \mathcal{U}_{\mathbb{S}^{d-1}}(L(t))] \in (0, \|p\|_\infty]$ .

Let us comment on Theorem 6.

**Remark 7** The right-hand side of (7) depends on  $p$  by

$$r_p := \sup_{t>0} [t \cdot \mathcal{U}_{\mathbb{S}^{d-1}}(L(t))] / \|p\|_\infty.$$

Observe that the decreasing level set function  $t \mapsto \mathcal{U}_{\mathbb{S}^{d-1}}(L(t))$  determines crucially the size of  $r_p \in (0, 1]$ , cf. Roberts and Rosenthal (1999); Natarovskii et al. (2021b) where it also appears differently in the characterization of convergence statements of slice sampling.

**Remark 8** The statement of the theorem contains the fact that for  $\|p\|_\infty < \infty$  we have  $r_p > 0$ , such that the right-hand side of (7) converges exponentially to zero. We provide an example where  $r_p$  is computed explicitly. For  $\delta \in (0, 1)$ ,  $S \subseteq \mathbb{S}^{d-1}$  open and  $\mathcal{U}_{\mathbb{S}^{d-1}}(S) = \gamma \in (0, 1]$  consider  $p(x) = \mathbb{1}_S(x) + \delta \cdot \mathbb{1}_{\mathbb{S}^{d-1} \setminus S}(x)$ . Note that for the corresponding level sets we have  $\mathcal{U}_{\mathbb{S}^{d-1}}(L(t)) = \mathbb{1}_{(0, \delta)}(t) + \gamma \cdot \mathbb{1}_{[\delta, 1)}(t)$  which implies  $r_p = \max\{\gamma, \delta\}$ .

**Remark 9** We can interpret the ideal geodesic slice sampler as Hit-and-run on the sphere. The Hit-and-run algorithm has been introduced for approximate sampling of distributions on  $\mathbb{R}^d$  (see Bélisle et al., 1993). A transition of the algorithm that starts in  $x \in \mathbb{R}^d$  is performed in the following way: A direction  $v$  is chosen uniformly at random in the unit ball centered around  $x$  to construct a straight line  $\ell$  through  $x$  in direction  $v$ . Then the next point is chosen w.r.t. the distribution of interest restricted to the line  $\ell$ . Since on the

sphere straight lines correspond to great circles, ideal geodesic slice sampling can be considered as Hit-and-run where simulating the target distribution restricted to the great circle is performed by slice sampling. Investigations on the performance of the Hit-and-run algorithm in  $\mathbb{R}^d$  w.r.t. the dimension attracted a lot of attention, cf. Lovász and Vempala (2007). Regarding this aspect note that for  $\varepsilon \in (0, 1)$  we require  $n \geq \sqrt{2(d-1)\pi} r_p^{-1} \log \varepsilon^{-1}$  for achieving  $\sup_{x \in \mathbb{S}^{d-1}} d_{tv}(H^n(x, \cdot), \pi) < \varepsilon$ , which illuminates a moderate dependence on  $d$ .

In the proof of Theorem 6 we apply Meyn and Tweedie (2009, Theorem 16.2.4). For the convenience of the reader we provide a reformulation of the relevant parts of this result.

**Lemma 10 (Meyn and Tweedie, 2009, Theorem 16.2.4)** *Let  $P : \mathbb{S}^{d-1} \times \mathcal{B}(\mathbb{S}^{d-1}) \rightarrow [0, 1]$  be a Markov kernel with stationary probability measure  $\eta$ . Assume there exists a non-zero measure  $\nu$  on  $(\mathbb{S}^{d-1}, \mathcal{B}(\mathbb{S}^{d-1}))$  such that  $P(x, A) \geq \nu(A)$  for all  $x \in \mathbb{S}^{d-1}$  and all  $A \in \mathcal{B}(\mathbb{S}^{d-1})$ . Then*

$$\sup_{x \in \mathbb{S}^{d-1}} d_{tv}(P^n(x, \cdot), \eta) \leq (1 - \nu(\mathbb{S}^{d-1}))^n, \quad \forall n \in \mathbb{N}.$$

We add one more auxiliary result which is proven in Appendix D.

**Lemma 11** *For  $x \in \mathbb{S}^{d-1}$  and  $A \in \mathcal{B}(\mathbb{S}^{d-1})$  we have*

$$\int_0^\pi \int_{\mathbb{S}_x^{d-2}} \mathbb{1}_A(\gamma_{(x,v)}(\theta)) \mathcal{U}_{\mathbb{S}_x^{d-2}}(dv) d\theta \geq \frac{\sqrt{2\pi}}{\sqrt{d-1}} \mathcal{U}_{\mathbb{S}^{d-1}}(A).$$

Now we turn to proof of the theorem:

**Proof (Proof of Theorem 6.)** Let  $x \in \mathbb{S}^{d-1}$  and  $s \in (0, \|p\|_\infty)$  such that  $L(s)$  is open and non-empty. Observe that for all  $v \in \mathbb{S}_x^{d-2}$  and  $\theta \in [0, 2\pi)$  with  $\gamma_{(x,v)}(\theta) \in L(s)$  holds

$$\frac{1}{p(x)} \int_0^{p(x)} \mathbb{1}_{[0, p(\gamma_{(x,v)}(\theta))]}(t) dt = \min \left\{ 1, \frac{p(\gamma_{(x,v)}(\theta))}{p(x)} \right\} \geq \frac{s}{\|p\|_\infty}. \quad (8)$$

Observe that  $L(x, v, t) \subseteq [0, 2\pi)$  such that  $\lambda(L(x, v, t)) \leq 2\pi$  for all  $v \in \mathbb{S}_x^{d-2}$  and all  $t \in (0, \infty)$ . Then, using Lemma 11 this implies

$$\begin{aligned} H(x, A) &= \frac{1}{p(x)} \int_0^{p(x)} \int_{\mathbb{S}_x^{d-2}} \frac{1}{\lambda(L(x, v, t))} \int_{L(x, v, t)} \mathbb{1}_A(\gamma_{(x,v)}(\theta)) d\theta \mathcal{U}_{\mathbb{S}_x^{d-2}}(dv) dt \\ &\geq \frac{1}{p(x)} \int_0^{p(x)} \int_{\mathbb{S}_x^{d-2}} \frac{1}{\lambda(L(x, v, t))} \int_{L(x, v, t)} \mathbb{1}_{A \cap L(s)}(\gamma_{(x,v)}(\theta)) d\theta \mathcal{U}_{\mathbb{S}_x^{d-2}}(dv) dt \\ &\geq \frac{1}{2\pi} \int_{\mathbb{S}_x^{d-2}} \int_0^{2\pi} \mathbb{1}_{A \cap L(s)}(\gamma_{(x,v)}(\theta)) \frac{1}{p(x)} \int_0^{p(x)} \mathbb{1}_{[0, p(\gamma_{(x,v)}(\theta))]}(t) dt d\theta \mathcal{U}_{\mathbb{S}_x^{d-2}}(dv) \\ &\stackrel{(8)}{\geq} \frac{s}{2\pi \|p\|_\infty} \int_0^\pi \int_{\mathbb{S}_x^{d-2}} \mathbb{1}_{A \cap L(s)}(\gamma_{(x,v)}(\theta)) \mathcal{U}_{\mathbb{S}_x^{d-2}}(dv) d\theta \geq \frac{s \mathcal{U}_{\mathbb{S}^{d-1}}(A \cap L(s))}{\sqrt{2\pi} \sqrt{d-1} \|p\|_\infty}, \end{aligned}$$

for all  $A \in \mathcal{B}(\mathbb{S}^{d-1})$ . By Lemma 10 this implies

$$\sup_{x \in \mathbb{S}^{d-1}} d_{tv}(H^n(x, \cdot), \pi) \leq \left( 1 - \frac{s \mathcal{U}_{\mathbb{S}^{d-1}}(L(s))}{\sqrt{2\pi} \sqrt{d-1} \|p\|_\infty} \right)^n$$

for any  $s > 0$ . Taking the infimum over  $s > 0$  on the right hand-side gives (7). By the lower semicontinuity of  $p$  we have that  $L(s)$  is open and non-empty, such that  $\mathcal{U}_{\mathbb{S}^{d-1}}(L(s)) \in (0, 1]$  for all  $s \in (0, \|p\|_\infty)$ . This implies  $0 < s \mathcal{U}_{\mathbb{S}^{d-1}}(L(s)) < \|p\|_\infty$ , which provides the final claim.  $\blacksquare$

### 3.2 Geodesic Shrinkage Slice Sampling.

Now we modify the ideal geodesic slice sampler by replacing the acceptance/rejection step of Algorithm 2 by a shrinkage procedure that has been also used in elliptical slice sampling (see Murray et al., 2010) and originates in Neal’s bracketing procedure on the interval  $[0, 2\pi)$  (see Neal, 2003). We pick candidates from subsets of  $[0, 2\pi)$  that shrink until an accepted sample is generated. Intuitively, this strategy reduces the number of rejections per iteration, because candidates will be drawn from nested intervals that contain a neighborhood of the current state. Note that this approach can still be viewed as a realization of the procedure discussed in Section 2.3 in the sense of Remark 4.

In Algorithm 3 we provide the shrinkage procedure as subroutine that is called as  $\text{shrink}(x, v, t)$  with input  $x \in \mathbb{S}^{d-1}$ ,  $v \in \mathbb{S}_x^{d-2}$  and level  $t \in (0, p(x))$ . Roughly, it generates a point from a specified geodesic level set  $L(x, v, t)$  by drawing points uniformly from a segment of (one winding) of the great circle  $\gamma_{(x,v)}$  until we hit  $L(x, v, t)$ , while the rejected points are used to successively shrink the segment of the great circle. We work with this procedure as a black box by encapsulating it in the distribution of its output. Considering

---

**Algorithm 3** Shrinkage procedure, called as  $\text{shrink}(x, v, t)$ .

---

**input:** current state  $x \in \mathbb{S}^{d-1}$ , direction  $v \in \mathbb{S}_x^{d-2}$ , level  $t \in (0, p(x))$

**output:** parameter  $\theta \in L(x, v, t)$

- 1: Draw  $\Theta \sim \mathcal{U}_{(0, 2\pi)}$ , call the result  $\theta$ .
  - 2: Set  $\theta_{\min} = \theta - 2\pi$  and set  $\theta_{\max} = \theta$ .
  - 3: **while**  $p(\cos(\theta)x + \sin(\theta)v) \leq t$  **do**
  - 4:   **if**  $\theta < 0$  **then**
  - 5:     Set  $\theta_{\min} = \theta$ .
  - 6:   **else**
  - 7:     Set  $\theta_{\max} = \theta$ .
  - 8:   **end if**
  - 9:   Draw  $\Xi \sim \mathcal{U}_{(\theta_{\min}, \theta_{\max})}$ , call the result  $\theta$ .
  - 10: **end while**
- 

the subroutine of Algorithm 3 as random variable yields the following definition.

**Definition 12** For lower semi-continuous  $p$ , for  $x \in \mathbb{S}^{d-1}$ ,  $v \in \mathbb{S}_x^{d-2}$  and  $t \in (0, p(x))$  we set

$$Q_{x,v,t}(A) := \mathbb{P}((\text{shrink}(x, v, t) \bmod 2\pi) \in A), \quad \forall A \in \mathcal{B}([0, 2\pi)),$$

where  $\text{shrink}(x, v, t)$  is determined by Algorithm 3.

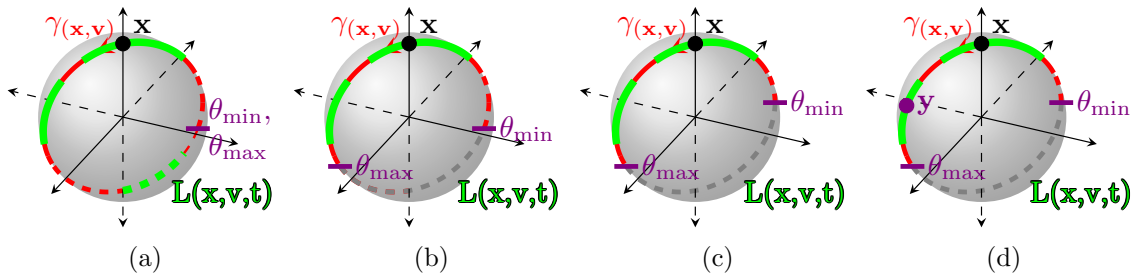


Figure 2: Shrinkage procedure of the geodesic shrinkage slice sampler. (a) First proposal is rejected. (b) Second proposal is rejected and becomes new right bound of the proposal interval. (c) Third proposal is rejected and becomes new left bound of the proposal interval. (d) Fourth proposal lies in geodesic level set  $L(x, v, t)$  and is accepted.

**Remark 13** *The distribution  $Q_{x,v,t}$  coincides with the kernel of the shrinkage procedure defined by Hasenpflug et al. (2024, Algorithm 2.2 with  $\theta_{in} = 0$ ,  $S = L(x, v, t)$ ). For details we refer to Appendix E. The lower semicontinuity of  $p$  ensures that  $Q_{x,v,t}$  is well-defined, cf. Hasenpflug et al. (2024). Intuitively, the openness of the superlevel sets guarantees that  $x$  lies in a subinterval of the image of the geodesic level set  $\gamma_{(x,v)}(L(x, v, t))$  for all  $v \in \mathbb{S}_x^{d-2}$  and all  $t \in (0, p(x))$ . Hence, while shrinking the sampling region on  $\gamma_{(x,v)}([0, 2\pi))$ , the probability to hit the level set for a given level  $t \in (0, p(x))$  is strictly positive.*

A single transition of the *geodesic shrinkage slice sampler* is presented in Algorithm 4 and for an illustration of the shrinkage scheme on a geodesic on  $\mathbb{S}^2$  we refer to Figure 2. To

---

**Algorithm 4** Geodesic shrinkage slice sampler.

---

**input:** current state  $x \in \mathbb{S}^{d-1}$

**output:** next state  $x'$

- 1: Draw  $V \sim \mathcal{U}_{\mathbb{S}_x^{d-2}}$ , call the result  $v$ .      {Perform Algorithm 5 with input  $x$ .}
  - 2: Draw  $T \sim \mathcal{U}_{(0,p(x))}$ , call the result  $t$ .
  - 3: Draw  $\Theta \sim Q_{x,v,t}$ , call the result  $\theta$ .      {Perform Algorithm 3 with input  $x, v, t$ .}
  - 4: Set  $x' = \cos(\theta)x + \sin(\theta)v$ .
- 

define the corresponding kernel  $\tilde{H}$ , we need the following auxiliary level set kernels  $\tilde{H}_t$ . Those correspond to drawing a random great circle through the starting point  $x$ , and then running the shrinkage procedure to generate a point from the intersection of the random great circle and the level set  $L(t)$ . That is, for  $x \in \mathbb{S}^{d-1}$ ,  $t \in (0, p(x))$  and  $A \in \mathcal{B}(\mathbb{S}^{d-1})$  we set

$$\tilde{H}_t(x, A) = \int_{\mathbb{S}_x^{d-2}} \int_{[0, 2\pi)} \mathbb{1}_A(\gamma_{(x,v)}(\theta)) Q_{x,v,t}(d\theta) \mathcal{U}_{\mathbb{S}_x^{d-2}}(dv)$$

and let

$$\tilde{H}(x, A) = \frac{1}{p(x)} \int_0^{p(x)} \tilde{H}_t(x, A) dt = \int_0^{p(x)} \tilde{H}_t(x, A) \mathcal{U}_{(0,p(x))}(dt).$$

In words, the kernel  $\tilde{H}$  can be described as first sampling a random level  $t$  below the current value of the unnormalized density  $p$  and then running the auxiliary kernel  $\tilde{H}_t$  associated to that random level.

**Remark 14** *Observe that due to the  $2\pi$ -periodicity of the geodesics on the sphere, we have*

$$\begin{aligned} & \cos(\text{shrink}(x, v, t) \bmod 2\pi)x + \sin(\text{shrink}(x, v, t) \bmod 2\pi)v \\ &= \cos(\text{shrink}(x, v, t))x + \sin(\text{shrink}(x, v, t))v \end{aligned}$$

for all  $x \in \mathbb{S}^{d-1}$ ,  $v \in \mathbb{S}_{d-2}^x$  and  $t \in (0, p(x))$ . Therefore, we may introduce this modulo operation when transitioning from the algorithmic formulation to a Markov kernel.

In Appendix E we prove that  $\tilde{H}$  is reversible with respect to our target distribution, which implies that  $\pi$  is the stationary distribution of this kernel. We obtain the following statement.

**Proposition 15** *For  $\pi$  defined as in (2) with lower semicontinuous  $p$ , the kernel  $\tilde{H}$  is reversible w.r.t.  $\pi$ .*

For the geodesic shrinkage slice sampler we also provide a statement about convergence to the target distribution.

**Theorem 16** *For  $p$  being lower semicontinuous with  $\|p\|_\infty < \infty$  we have*

$$\sup_{x \in \mathbb{S}^{d-1}} d_{tv} \left( \tilde{H}^n(x, \cdot), \pi \right) \leq \left( 1 - \frac{\sup_{t>0} [t \cdot \mathcal{U}_{\mathbb{S}^{d-1}}(L(t))]}{\sqrt{2\pi}\sqrt{d-1} \|p\|_\infty} \right)^n, \quad \forall n \in \mathbb{N}, \quad (9)$$

where  $\sup_{t>0} [t \cdot \mathcal{U}_{\mathbb{S}^{d-1}}(L(t))] \in (0, \|p\|_\infty]$ .

We follow the same strategy of proof as in Theorem 6, i.e., we show that the whole state space is a small set for  $\tilde{H}$  and then apply Lemma 10. To this end, the crucial idea is to estimate the distribution  $Q_{x,v,t}$  by its restriction to the event that the loop in Algorithm 3 terminates after the first iteration.

**Proof** (*Proof of Theorem 16.*) For arbitrary  $x \in \mathbb{S}^{d-1}$ ,  $s \in (0, \|p\|_\infty)$  with  $L(s)$  being open and non-empty, for any  $v \in \mathbb{S}_x^{d-2}$  and  $\theta \in [0, 2\pi)$  with  $\gamma_{(x,v)}(\theta) \in L(s)$  we have (cf. (8)) that

$$\frac{1}{p(x)} \int_0^{p(x)} \mathbb{1}_{[0,p(\gamma_{(x,v)}(\theta))]}(t) dt \geq \frac{s}{\|p\|_\infty}. \quad (10)$$

Moreover, for all  $t \in (0, p(x))$  we obtain with  $\Theta \sim \mathcal{U}_{(0,2\pi)}$  that

$$Q_{x,v,t}(B) \geq \mathbb{P}(\Theta \in B \cap L(x, v, t)) = \frac{1}{2\pi} \lambda(B \cap L(x, v, t)), \quad B \in \mathcal{B}([0, 2\pi)). \quad (11)$$

Then

$$\begin{aligned} \tilde{H}(x, A) & \stackrel{(11)}{\geq} \frac{1}{p(x)} \int_0^{p(x)} \int_{\mathbb{S}_x^{d-2}} \frac{1}{2\pi} \int_{L(x,v,t)} \mathbb{1}_A(\gamma_{(x,v)}(\theta)) d\theta \mathcal{U}_{\mathbb{S}_x^{d-2}}(dv) dt \\ & \geq \frac{1}{2\pi} \int_{\mathbb{S}_x^{d-2}} \int_{[0,2\pi)} \mathbb{1}_{A \cap L(s)}(\gamma_{(x,v)}(\theta)) \frac{1}{p(x)} \int_0^{p(x)} \mathbb{1}_{[0,p(\gamma_{(x,v)}(\theta))]}(t) dt d\theta \mathcal{U}_{\mathbb{S}_x^{d-2}}(dv) \\ & \stackrel{(10)}{\geq} \frac{s}{2\pi \|p\|_\infty} \int_{\mathbb{S}_x^{d-2}} \int_{[0,2\pi)} \mathbb{1}_{A \cap L(s)}(\gamma_{(x,v)}(\theta)) d\theta \mathcal{U}_{\mathbb{S}_x^{d-2}}(dv) \geq \frac{s \cdot \mathcal{U}_{\mathbb{S}^{d-1}}(A \cap L(s))}{\sqrt{2\pi}\sqrt{d-1} \|p\|_\infty}, \end{aligned}$$

where the last inequality follows by Lemma 11. Therefore, by Lemma 10 and by taking the infimum over  $s > 0$  on the right hand-side we get

$$\sup_{x \in \mathbb{S}^{d-1}} d_{tv} \left( \tilde{H}^n(x, \cdot), \pi \right) \leq \left( 1 - \frac{\sup_{t>0} [t \cdot \mathcal{U}_{\mathbb{S}^{d-1}}(L(t))]}{\sqrt{2\pi}\sqrt{d-1} \|p\|_\infty} \right)^n, \quad \forall n \in \mathbb{N}.$$

Finally, note that  $\sup_{t>0} [t \cdot \mathcal{U}_{\mathbb{S}^{d-1}}(L(t))] \in (0, \|p\|_\infty]$  follows already from Theorem 6. ■

We comment on the result.

**Remark 17** *Note that the right hand-side of (9) coincides with the right hand-side of (7) stated in Theorem 6 that addressed the uniform ergodicity statement for ideal slice sampling. This is due to the proof technique, since in the small set estimate, we lower bound both kernels with the same expression of Lemma 11. Intuitively, it is clear that  $\sup_{x \in \mathbb{S}^{d-1}} d_{tv}(H^n(x, \cdot), \pi)$  is smaller than  $\sup_{x \in \mathbb{S}^{d-1}} d_{tv}(\tilde{H}^n(x, \cdot), \pi)$ , since the shrinkage procedure just adaptively imitates the acceptance/rejection step of the ideal one to gain computational efficiency. Exactly this gain in efficiency leads in applications to a potentially better accuracy to cost ratio, although the performance per Markov chain transition may be worse. We also point out that essentially Remark 7 and Remark 8 apply for Theorem 16 as well.*

## 4 Numerical Illustrations

We demonstrate geodesic slice sampling on the sphere for approximate sampling on various distributions on the sphere and compare it to tailor-made and general purpose MCMC algorithms including random-walk Metropolis-Hastings (RWMH) and Hamiltonian Monte Carlo (HMC). The RWMH algorithm on the sphere is very similar to the standard RWMH, for details refer to Appendix F. Lan et al. (2014) have developed a modified version of HMC for sampling spherical distributions. The details of the HMC algorithm can be found in Appendix G. Both RWMH and HMC have a step-size parameter that is automatically tuned for each target, see Appendix H. For a prespecified sampler we denote by  $(x_n)_{n \in \mathbb{N}} \subset \mathbb{S}^{d-1}$  a realization of the corresponding Markov chain.

### 4.1 Bingham Distribution

In our first test, we aim to sample from the Bingham distribution (Mardia and Jupp, 2000) whose unnormalized density is defined as

$$p_{\text{Bing}}(x) = \exp(x^T A x) \tag{12}$$

for  $x \in \mathbb{S}^{d-1}$ . Without loss of generality, the matrix  $A \in \mathbb{R}^{d \times d}$  is symmetric such that we can transform the variables into the eigenbasis of  $A$ . In the following, we assume that the variables underwent this transformation by letting  $A = \text{diag}(\kappa_1, \dots, \kappa_d)$  where  $\kappa_1 \leq \kappa_2 \leq \dots \leq \kappa_d$  are the eigenvalues of  $A$ . Because the Bingham distribution is invariant under shifts of the diagonal of  $A$ , i.e., invariant under  $A \mapsto A + c \text{Id}_d$ , where  $c \in \mathbb{R}$  is some constant, we can let  $\kappa_1 = 0$ . The Bingham distribution is bimodal with symmetric modes at  $\pm u_d$  where  $u_d \in \mathbb{S}^{d-1}$  is the eigenvector of  $A$  with the largest eigenvalue  $\kappa_d$ .

The maximal value of the logarithm of the unnormalized probability density is  $\kappa_d$ , i.e.,  $\max_{x \in \mathbb{S}^{d-1}} \log p_{\text{Bing}}(x) = \kappa_d$ . Various algorithms for simulating the Bingham distribution have been proposed. The algorithm by Kent et al. (2018) is particularly attractive because it uses an acceptance/rejection sampler based on the angular central Gaussian (ACG) distribution as an envelope and is therefore straightforward to implement. We use this method as a baseline against which we compare our slice samplers as well as RWMH and HMC. We run the geodesic slice samplers on the sphere (geoSSS) as well as RWMH and HMC on two high-dimensional Bingham targets with  $d = 10$  and  $d = 50$ , respectively. For each target and sampling algorithm, we simulate the consecutive Markov chain realizations  $x_1, \dots, x_N$  with  $N = 10^5$  starting from the mode  $u_d$ . To explore the variability of all MCMC algorithms, we run 10 repetitions. The step-size parameter of the RWMH and HMC algorithm is tuned as described in Appendix H to achieve a reasonable average acceptance rate.

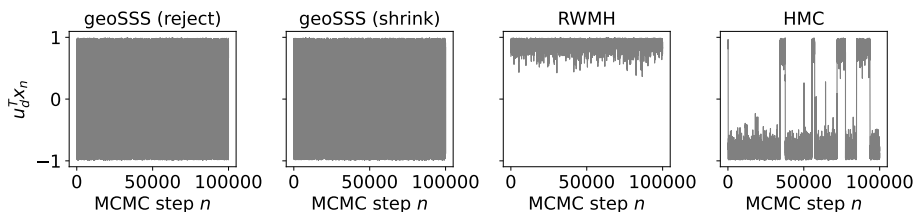


Figure 3: Traces of approximate samples from a Bingham distribution with  $d = 10$  and  $\kappa_d = 30$  projected onto one of both modes  $u_d$ .

The first Bingham target has  $d = 10$  and  $\kappa_d = 30$ . In Figure 3, we show traces of approximate Bingham samples projected onto the first mode, that is  $u_d^T x$ , which varies between 1 and  $-1$  and is expected to peak somewhat below these extreme values that correspond to both modes. As is evident from the trace plots, both variants of geodesic slice sampling on the sphere find both modes of the Bingham distribution and rapidly jump between them. RWMH, on the other hand, does not escape from the mode in which the chain was started and therefore only finds a single mode. HMC also finds the second mode, but only jumps occasionally between the two modes.

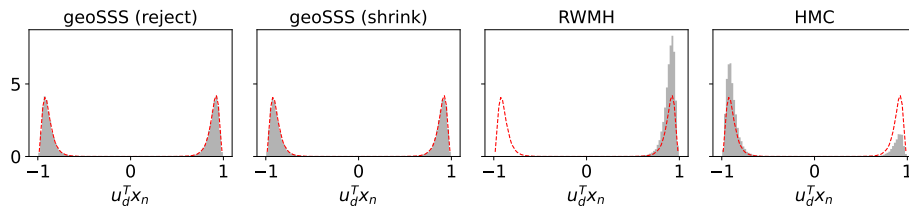


Figure 4: Histograms of approximate Bingham samples with  $d = 10$  and  $\kappa_d = 30$  projected on the first mode obtained with each MCMC method are shown in grey. The red dashed line indicates the baseline obtained with the acceptance/rejection sampler of Kent et al. (2018).

The insufficient sampling by RWMH and HMC results in an incorrect exploration of the modes, which should be populated equally. This is illustrated in Figure 4 which also shows

the distribution of  $u_d^T x$  obtained by the aforementioned acceptance/rejection method (see Kent et al., 2018). The histograms obtained with the geodesic slice samplers closely match the baseline, whereas RWMH completely misses the second mode and HMC misrepresents the probability mass under the modes.

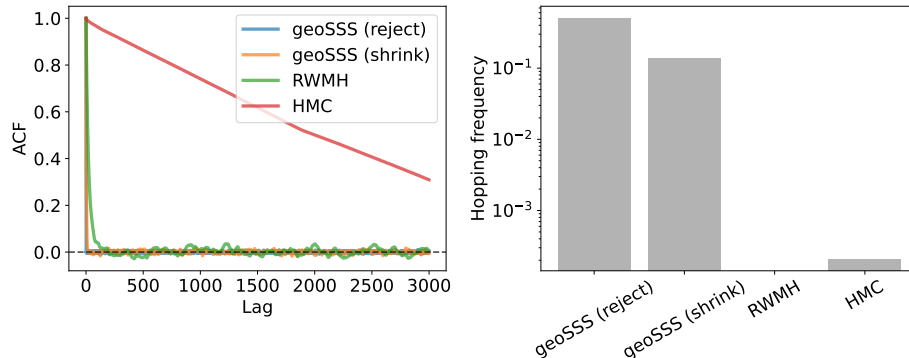


Figure 5: Left: Autocorrelation analysis of  $x \mapsto u_d^T x$  with respect to approximate samples from a Bingham distribution with  $d = 10$  and  $\kappa_d = 30$ . Right: Estimated hopping frequency between both modes of the Bingham distribution. Note that the hopping frequency is shown on a logarithmic axis.

Figure 5 shows the autocorrelation function (ACF) of  $u_d^T x$  for the four MCMC samplers. We see a rapid decorrelation in case of both geodesic slice samplers; in fact, the ACF of rejection-based geoSSS drops to zero after a single step. Samples generated with RWMH decorrelate after roughly 200 MCMC steps, but the faster decorrelation (in comparison to HMC) is due to the fact that RWMH only explores a single mode. HMC finds both modes but shows a very slowly decaying ACF, because jumps between the two modes only occur very rarely. This is also reflected in the effective sample size (ESS). Due to the immediate decorrelation of samples generated with geoSSS using a rejection strategy, the *relative ESS*<sup>1</sup> is estimated to be 99.73 %. The shrinkage-based geoSSS obtains a relative ESS of 15.2 %, whereas RWMH and HMC achieve only very low relative ESS: 0.004 % and 0.01 %, respectively.

To quantify how rapidly the MCMC samplers mix between the two modes of the Bingham distribution, we estimated a *hopping frequency*, which we define as the average number of times the Markov chain jumps from one mode to the other, given by

$$\frac{1}{N-1} \sum_{n=1}^{N-1} \llbracket \text{sign}(u_d^T x_{n+1}) \neq \text{sign}(u_d^T x_n) \rrbracket, \quad (13)$$

where  $x_n$  is the realization of the  $n$ -th Markov chain sample,  $N$  the total number of steps and  $\llbracket \cdot \rrbracket$  denotes the Iverson bracket<sup>2</sup>.

Figure 5 shows the estimated hopping frequencies. As expected, the rejection-based geoSSS shows the highest number of oscillations between both modes with approximately

<sup>1</sup>The relative ESS is just the ESS divided by the total number of performed MCMC steps, in our experiments  $10^5$ .

<sup>2</sup>For proposition  $S$  it holds that  $\llbracket S \rrbracket = 1$  if  $S$  is a true and  $\llbracket S \rrbracket = 0$  otherwise.



50% hopping frequency, whereas the shrinkage-based geoSSS tends to jump only every seventh step to the other mode. This behavior is expected, because the geodesic level set always contains both modes with equal probability. Therefore, the rejection sampling strategy finds each mode with equal probability, independent of what the current state of the Markov chain is. The shrinkage-based approach has a higher chance to stay in the vicinity of the current state.

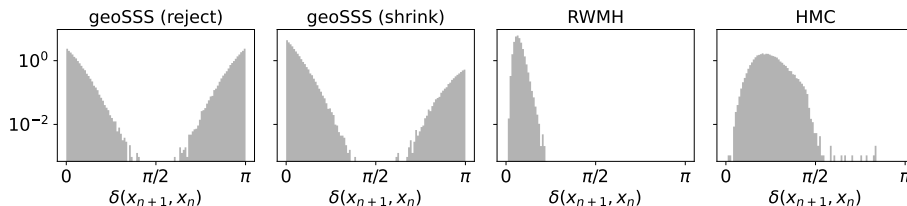


Figure 6: Geodesic distance (log-scale) between successive approximate samples for a Bingham distribution with  $d = 10$  and  $\kappa_d = 30$ .

Another quality measure is the geodesic or great circle distance between successive samples given as

$$\delta(x_{n+1}, x_n) := \arccos(x_{n+1}^T x_n).$$

An efficient MCMC algorithm should explore the sphere rapidly by making large leaps from one sample to the next. Again, we see in Fig. 6 a superior performance of geoSSS. The RWMH algorithm achieves only small jumps. As expected, HMC moves more rapidly over the sphere compared to RWMH, but it still cannot compete with the geodesic slice samplers.

We also run similar tests on a more challenging Bingham target with  $d = 50$  and  $\kappa_d = 300$ , i.e., the dimension of the sample space is much larger and the distribution is more concentrated. We observe the same trends as before. Supplementary Figure A1 shows the distribution of samples projected onto the first mode. Now, both RWMH and HMC are stuck in the first mode and fail to find the second mode, whereas the geodesic slice samplers represent both modes accurately. The ACF of HMC outperforms RWMH as expected (see Supplementary Fig. A2), but still the geodesic slice samplers show a faster decorrelation than HMC resulting in a higher effective sample size. Since no jumps occur during the entire run of RWMH and HMC, their hopping frequencies are estimated to be smaller than  $10^{-5}$ , whereas geoSSS still achieves an acceptable jump rate (see Appendix Fig. A2). The rejection-based geoSSS clearly outperforms the shrinkage strategy on this target by achieving a higher hopping rate and as a consequence also a more favorable distribution of step sizes  $\delta(x_{n+1}, x_n)$  (see Appendix Fig. A3).

## 4.2 Mixture of von Mises-Fisher Distributions

We test the slice samplers as well as RWMH and HMC also on a  $K$ -component mixture model of von Mises-Fisher (vMF) distributions in  $d$  dimensions. The vMF distribution is defined by the unnormalized density

$$p_{\text{vMF}}(x; \kappa, \mu) = \exp(\kappa \mu^T x), \quad x \in \mathbb{S}^{d-1}, \quad (14)$$

where  $\kappa > 0$  is the concentration parameter and  $\mu \in \mathbb{S}^{d-1}$ . For  $K \in \mathbb{N}$  our target distribution is a particular mixture of vMF distributions where each component has the same weight  $1/K$  and concentration parameter  $\kappa$ , i.e., the corresponding unnormalized density takes the form

$$p_{\text{mix}}(x) = \frac{1}{K} \sum_{k=1}^K p_{\text{vMF}}(x; \kappa, \mu_k), \quad x \in \mathbb{S}^{d-1}, \quad (15)$$

where every  $\mu_k \in \mathbb{S}^{d-1}$  with  $k \in \{1, \dots, K\}$  is sampled w.r.t. the uniform distribution on the unit sphere and then fixed. To generate a baseline, we use the method by Wood (1994).

As before, we evaluate both geoSSS variants against RWMH and HMC on a 10-dimensional mixture of vMF distributions with  $K = 5$  mixture components on the unit sphere  $\mathbb{S}^9$ . We set  $\kappa = 100$  and draw  $10^6$  samples.

As a measure for the quality of approximate sampling we consider the distribution with which the samplers visit the  $K$  modes of the target mixture model (15). Ideally, this distribution should be uniform, because each component of the mixture has the same weight and concentration parameter. We contrast the empirical frequency  $q_k$  with which the  $k$ -th mode is visited by a sampler with the uniform distribution by using the Kullback-Leibler (KL) divergence

$$\text{KL}(q \mid p) := \sum_{k=1}^K q_k \log(q_k/p_k)$$

where  $p_k = 1/K$  is the ideal distribution. To estimate  $q_k$ , we assign samples  $x_n$  to the nearest of the  $K$  peaks based on the geodesic distance. This allows us to count how often each mode was visited by the Markov chain. A good MCMC sampler should produce  $q_k \approx 1/K$  resulting in  $\text{KL}(q \mid p) \approx 0$ . The more the KL divergence differs from the minimum value of zero, the greater is the mismatch between the ideal and empirical frequency of mode visits. Remarkably as seen from the right panel of Fig. 7, only the geoSSS variants achieve a small KL divergence. RWMH and HMC produce large KL divergences, indicating a poorer representation of the target distribution compared to geoSSS. Although RWMH is the fastest to decorrelate (see left panel of Fig. 7), it is unreliable as observed from the KL divergence result. The geoSSS variants decorrelate much faster as compared to HMC. This aligns with the observations from the marginal histograms (see Fig. 8). Both variants of geoSSS approximates the underlying mixture significantly better compared to HMC and especially RWMH which fails to approximate every component correctly. Furthermore, the great circle distance between successive samples (see Fig. 9) shows that the slice samplers explore the entire sphere again consistent with previous numerical tests.

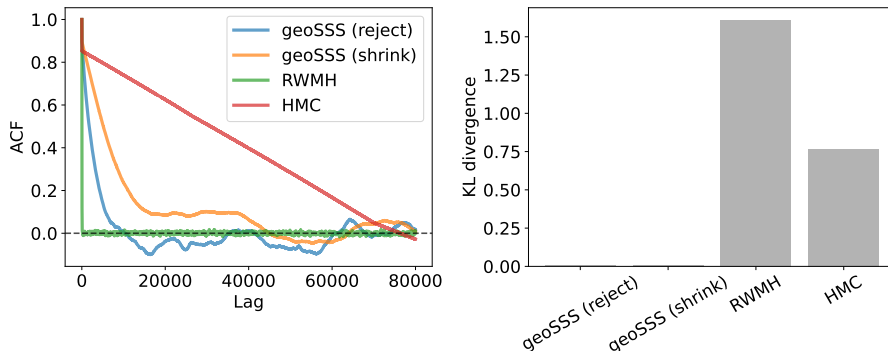


Figure 7: Left panel: ACF plotted for the first dimension from the 10-dimensional mixture of a vMF distribution. Right panel: KL divergence between the empirical and ideal frequency with which each mode is visited by the four MCMC samplers.

We further evaluate the performance of the samplers by fixing the components on the sphere and increasing the concentration parameter  $\kappa$  from 50 to 500, therefore making the distributions “spikier”. We estimate the effective sample size (ESS) for each method by considering 10 chains and  $10^6$  MCMC steps from the first dimension, resulting in ESS values per method for each  $\kappa$ . Left panel of Fig. 10 shows the estimated ESS for each of the four samplers as a function of the concentration parameter  $\kappa$ . Overall, we observe that sampling the mixture model becomes more challenging as the components become more concentrated with increasing  $\kappa$  for all methods. However, both geoSSS outperform RWMH and HMC, particularly for lower  $\kappa$  values. At large  $\kappa$  values, all samplers perform similarly poorly and fail to produce a reliable approximation of the target.

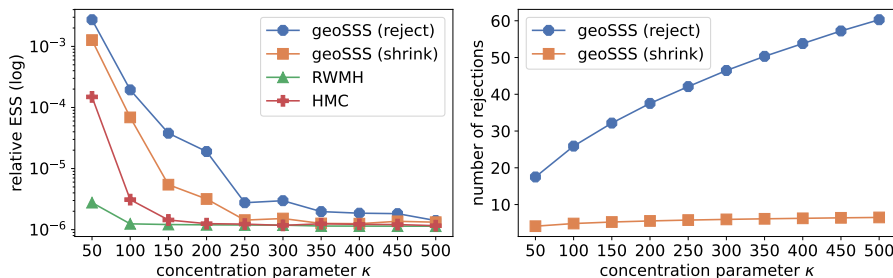


Figure 10: Comparing the MCMC samplers for the mixture of vMF distribution ( $d = 10$ ,  $K = 5$ ) by varying  $\kappa$  from 50 to 500; Left panel: Considering the first dimension, estimating the relative effective sample size (ESS) for 10 chains. Right panel: Number of rejections per MCMC step.

It is worth noting that the rejection-based geoSSS yields the highest ESS, albeit at the cost of generating a significantly larger number of rejected samples in comparison to the shrinkage-based geoSSS. This is demonstrated in the right panel of Fig. 10, where it is observed that the rejection-based geoSSS generates an increasingly larger number of rejected samples for higher values of  $\kappa$ . For instance, for  $\kappa = 50$ , approximately 17 rejections happen per MCMC step, while for  $\kappa = 500$ , around 60 rejections occur. On the other hand, the

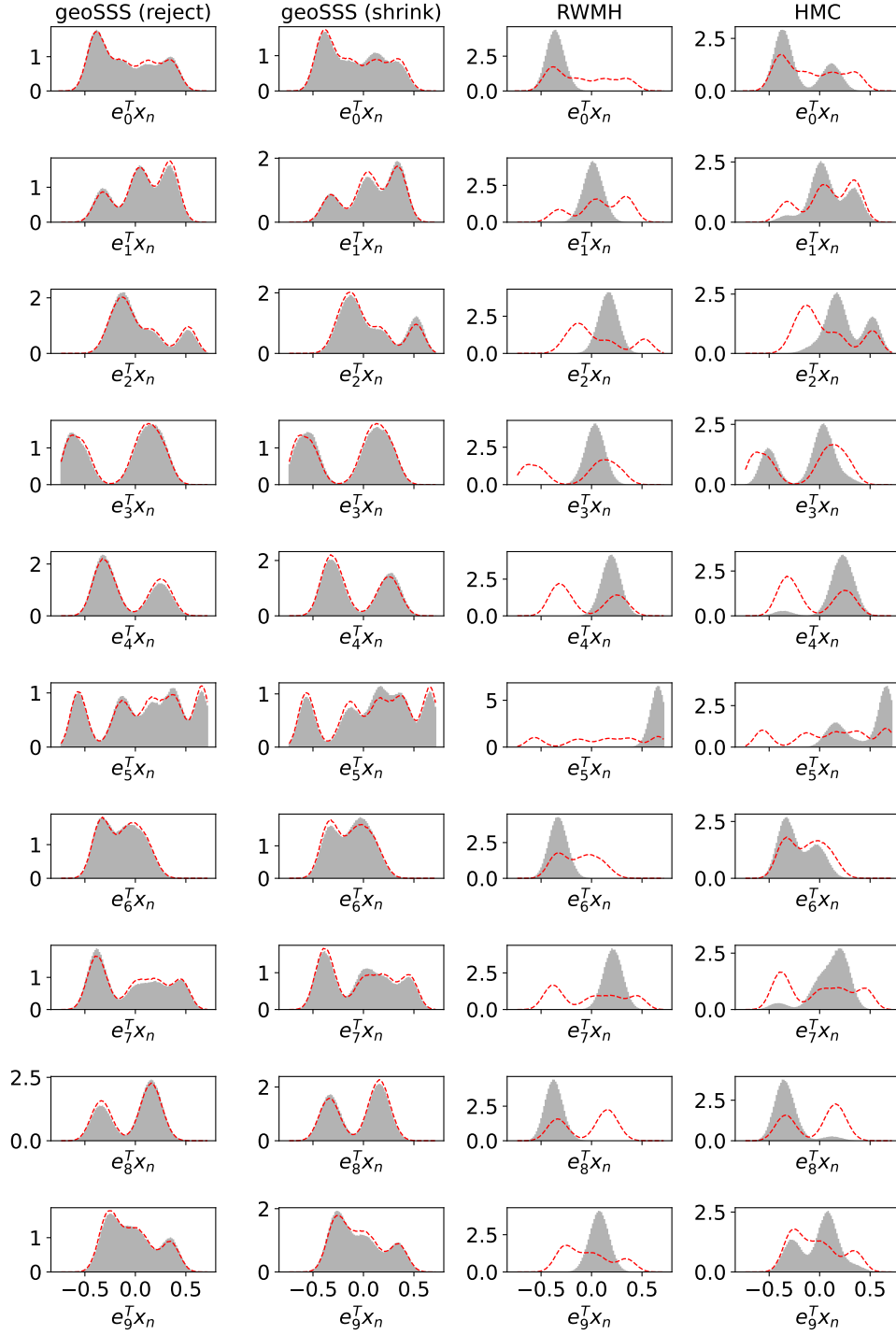


Figure 8: Marginal distributions (shown in grey) for the mixture of vMF distribution ( $d = 10, \kappa = 100, K = 5$ ) where columns corresponds to MCMC methods and rows correspond to the dimension of the marginal. The red dashed line indicates the baseline obtained with the acceptance/rejection sampler (see Wood, 1994).

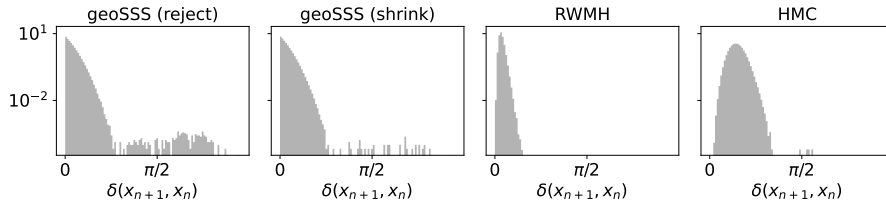


Figure 9: Geodesic distance (log-scale) between successive approximate samples for the mixture of vMF distribution ( $d = 10$ ,  $K = 5$  and  $\kappa = 100$ ).

number of rejections for the shrinkage-based geoSSS increases at a much slower rate with  $\kappa$ . It can be seen here that for  $\kappa = 50$ , we have approximately 4 rejections per MCMC step, and for  $\kappa = 500$ , approximately just 6 rejections per MCMC step occur. Thus, selecting between the two samplers necessitates a trade-off between computational requirements and accuracy. The number of rejections directly determines the number of log probability evaluations and thereby the computational costs of the slice samplers. RWMH and HMC, on the other hand, have a fixed computational budget per MCMC step. In case of RWMH, one step requires a single log probability evaluation, whereas an HMC step involves one log probability evaluation as well as multiple gradient evaluations, one for each leapfrog step. In our settings, we use 10 leapfrog integration steps. Among the four MCMC strategies studied here, RWMH has the lowest computational costs, but also the smallest ESS. The computational costs of shrinkage-based geoSSS is smaller than the costs of HMC, nevertheless geoSSS also performs better in terms of the other evaluation criteria in comparison to HMC.

### 4.3 Curved Distribution on the 2-Sphere

HMC is expected to show superior performance on target densities that accumulate ‘mass’ along narrow connected regions. To study such a sampling problem, we define a spherical distribution along a curve. The curve is created by picking 10 points uniformly distributed on the 2-sphere and connecting them such that the overall distance is shortest (this is done by solving a small traveling salesman problem). We use spherical linear interpolation (slerp) to interpolate between two successive points  $x, y \in \mathbb{S}^{d-1}$ , i.e., we apply

$$t \mapsto \frac{\sin(\theta(1-t))x + \sin(\theta t)y}{\sin(\theta)},$$

where  $\theta = \arccos(x^T y)$ , cf. Hanson (1995). If  $\mu(t)$  with  $t \in [0, 1]$  is the curve obtained by concatenating the slerps between the 9 pairs of successive points, then we define the spherical distribution with unnormalized density

$$p(x) = \exp \left\{ \kappa \max_{t \in [0, 1]} x^T \mu(t) \right\}, \quad x \in \mathbb{S}^{d-1}, \quad (16)$$

which we also call curved von Mises-Fisher distribution (curved vMF).

The maximum of  $x^T \mu(t)$  for a single slerp can be computed in closed form. The total maximum over the entire curve is the maximum over the maxima of slerps connecting two successive points. The probability distribution determined by (16) concentrates ‘mass’ around the curve. As in the case for the standard vMF distribution, the parameter  $\kappa$  controls the concentration. In our sampling tests, we choose  $\kappa = 300$ . We run all four

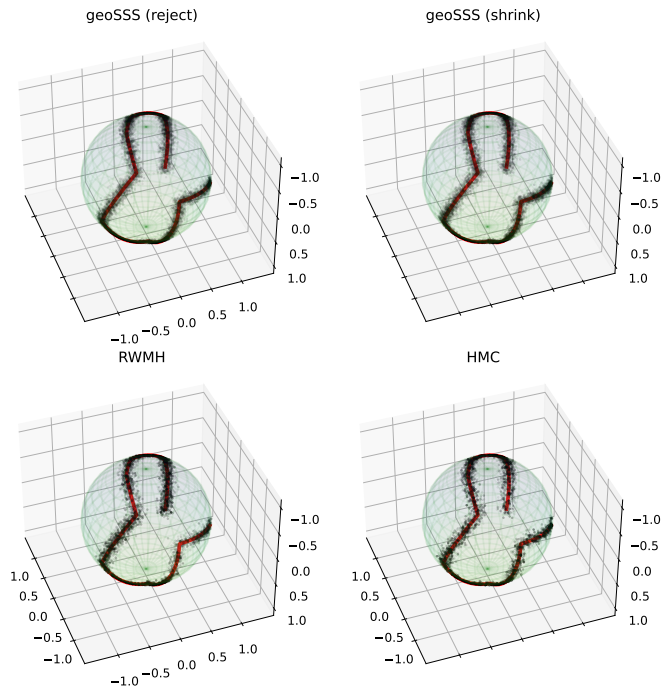


Figure 11: Samples of the four different MCMC samplers targeting a curved vMF on the 2-sphere are shown as black dots. The red curve is generated by positioning 10 points uniformly distributed on the sphere and interpolating between them using slerp. The concentration parameter is  $\kappa = 300$ .

samplers on targeting the corresponding curved vMF. Rejection-based geoSSS and HMC takes roughly similar run duration, HMC taking slightly longer. However, almost twice as long as shrinkage-based geoSSS. RWMH is by far the fastest method. Refer Appendix J for run times.

Figure 11 shows the samples of the four Markov chain approaches of the first 10000 MCMC iterations. RWMH fails to explore the entire curve. On the other hand, the slice samplers and, as expected, HMC manage to explore the entire curve fairly uniformly. To measure the discrepancy between the discretized target and the histogram generated by a sampling procedure, we use KL divergence as a metric. Right panel of Fig. 12 shows that the two slice samplers achieve the lowest KL values, surprisingly better than HMC, and thus produce a representation of the target that is more faithful to the true distribution than what RWMH is able to achieve. RWMH also shows the worst ACF with a very slow decay (left panel Fig. 12). Among the other three samplers, the slice samplers outperform HMC in that they decorrelate more rapidly. As expected, the rejection-based geoSSS shows the fastest decorrelation. The distribution of distances between successive samples also disfavors RWMH (Fig. 13). Both geoSSS variants show a peak at very short distances. HMC performs better in that it avoids minor changes and produces larger distances. Nevertheless the slice samplers reach out to larger distances covering the entire range of great-circle distance from 0 to  $\pi$  more often than HMC.

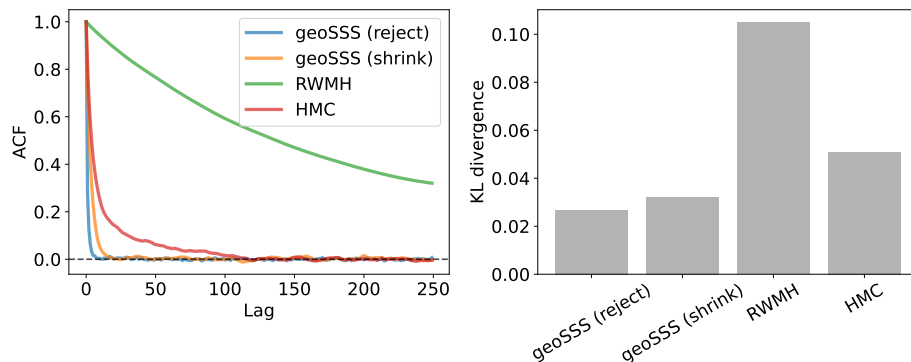


Figure 12: Left panel: ACF plotted for the first dimension based on  $10^5$  samples. Right panel: KL divergence between a discretized version of the curved vMF target and a histogram compiled from the MCMC samples.

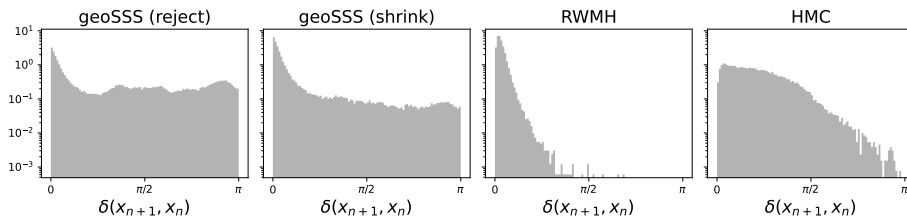


Figure 13: Geodesic distance (log-scale) between successive approximate samples for the curved von Mises-Fisher distribution (16).

## 5 Summary

We introduce two slice sampling based MCMC-methods on the sphere, the ideal geodesic and geodesic shrinkage slice samplers, that use movements on great circles. For the Markov kernels of both samplers we are able to establish reversibility and explicit convergence statements under mild assumptions. In numerical experiments we see that in particular for moderately concentrated target distributions with a moderate number of dimensions our slice samplers perform well and can compete with RWMH and HMC on the sphere, while having the additional advantage of being free of tuning parameters. For multimodal target distributions we observe that the ideal geodesic slice sampler and the geodesic shrinkage slice sampler even outperform RWMH and HMC. However, we observe that the performance of our methods, just as for RWMH and HMC, deteriorates for increasing concentration of the target distribution, and it is to be expected that the same happens for increasing dimension. This dependence on concentration and dimension already appears in Theorem 6 and Theorem 16. Regarding the comparison between the two geodesic slice samplers, the ideal version seems to outperform the shrinkage based sampler in terms of Markov chain transitions. However, this comes with a (significantly) greater computational cost per transition.

## Acknowledgments and Disclosure of Funding

All authors are grateful for the support of the DFG within project 432680300 – SFB 1456 subprojects A05 and B02. We also thank Philip Schär for valuable comments and discussions about the topic. M. Habeck and S. Kodgirwar gratefully acknowledge funding by the Carl Zeiss Foundation within the program “CZS Stiftungsprofessuren” and by the German Research Foundation (DFG) within grant HA 5918/4-1.

## Code Availability

The implementation of our geoSSS algorithms as well as RWMH (see Appendix F) and spherical HMC (Lan et al., 2014) on the sphere as well as scripts for all the numerical illustrations are compiled in our package labeled “GeoSSS”, accessible at this GitHub repository <https://github.com/microscopic-image-analysis/geosss>. The numerical illustration results computed from the “/scripts” directory from the repository are uploaded at Zenodo <https://doi.org/10.5281/zenodo.8287302>.



---

**Algorithm 5** Sampling from  $\mathcal{U}_{\mathbb{S}_x^{d-2}}$ .

---

**input** point  $x \in \mathbb{S}^{d-1}$

**output** sample  $v$  from  $\mathcal{U}_{\mathbb{S}_x^{d-2}}$

- 1: Draw  $Y \sim \mathcal{N}(0, \text{Id}_d)$ , call the result  $y$ .
  - 2: Set  $z = y - (x^T y)x$  and  $v = z/\|z\|$ .
- 

## Appendix A. Simulation of $\mathcal{U}_{\mathbb{S}_x^{d-2}}$

Implementing the slice sampling algorithms proposed in this paper involves sampling from  $\mathcal{U}_{\mathbb{S}_x^{d-2}} = \frac{1}{\omega_{d-2}} \mu_x$  for  $x \in \mathbb{S}^{d-1}$ . A scheme for performing it is provided in Algorithm 5 and justified as follows. It exploits that  $\mathbb{S}_x^{d-2}$  can be interpreted “as tilted  $\mathbb{S}^{d-1}$ , such that it lies in the  $(d-1)$ -dimensional hyperplane orthogonal to  $x$ ”. We formalize the arguments and require further objects. For  $x \in \mathbb{S}^{d-1}$  let

$$E_x := \{y \in \mathbb{R}^d \mid y^T x = 0\}$$

be the  $(d-1)$ -dimensional hyperplane with normal vector  $x$ . Since this is a  $(d-1)$ -dimensional subvectorspace of  $\mathbb{R}^d$ , we can choose an orthonormal basis  $e_1^{(x)}, \dots, e_{d-1}^{(x)} \in E_x$  of  $E_x$ . The isometric mapping

$$\varphi_x : \mathbb{R}^{d-1} \rightarrow E_x, \quad (y_1, \dots, y_{d-1}) \mapsto \sum_{i=1}^{d-1} y_i e_i^{(x)} \quad (17)$$

describes the rotation of  $\mathbb{R}^{d-1}$  into  $E_x$ . Therefore it assigns the unit sphere in  $\mathbb{R}^{d-1}$  to the unit sphere in  $E_x$ , i.e.,  $\varphi_x(\mathbb{S}^{d-2}) = \mathbb{S}_x^{d-2}$ . Isometries preserve volume, such that

$$\mu_x(A) = \sigma_{d-2}(\varphi_x^{-1}(A)), \quad \forall A \in \mathcal{B}(\mathbb{S}_x^{d-2}), \quad (18)$$

provides the crucial relation between the volume measure on  $\mathbb{S}^{d-2}$  and the volume measure  $\mu_x$  on the tilted version  $\mathbb{S}_x^{d-2}$ , (see also Munkres, 1991, Exercise 25.4). In particular,  $\mu_x(\mathbb{S}_x^{d-2}) = \omega_{d-2}$ .

We prove the validity of Algorithm 5 based upon this relationship between  $\sigma_{d-2}$  and  $\mu_x$ . More detailed, for  $x \in \mathbb{S}^{d-1}$  we establish an expression for the mapping  $y \mapsto y - x^T y x$  in terms of  $\varphi_x$  that describes the projection of  $\mathbb{R}^d$  onto  $E_x$ . Then, we deduce that Algorithm 5 realizes a transformed normalized standard normally distributed random variable under the isometry  $\varphi_x$ . By (18) this implies the desired result formalized as follows.

**Lemma 18** *Let  $Y$  be a random variable distributed according to the  $d$ -dimensional standard normal distribution  $\mathcal{N}(0, \text{Id}_d)$ . Then, for any  $x \in \mathbb{S}^{d-1}$  we have  $\frac{Y - x^T Y x}{\|Y - x^T Y x\|} \sim \mathcal{U}_{\mathbb{S}_x^{d-2}}$ .*

**Proof** Let  $U \in \mathbb{R}^{d \times (d-1)}$  be the matrix with columns  $e_1^{(x)}, \dots, e_{d-1}^{(x)}$  and let  $\tilde{U} \in \mathbb{R}^{d \times d}$  be the matrix with columns  $e_1^{(x)}, \dots, e_{d-1}^{(x)}, x$ , where  $e_1^{(x)}, \dots, e_{d-1}^{(x)}$  are defined as above. Since  $e_1^{(x)}, \dots, e_{d-1}^{(x)}, x$  is an orthonormal basis of  $\mathbb{R}^d$ , we may write  $y \in \mathbb{R}^d$  as  $y = \sum_{i=1}^{d-1} \alpha_i e_i^{(x)} + \alpha_d x$  where  $\alpha := (\alpha_1, \dots, \alpha_d)^T = \tilde{U}^T y$ . Therefore, we have

$$y - x^T y x = \sum_{i=1}^{d-1} \alpha_i e_i^{(x)} = \varphi_x((\alpha_1, \dots, \alpha_{d-1})^T) = \varphi_x(U^T y).$$

Since  $Y \sim \mathcal{N}(0, \text{Id}_d)$  and  $\tilde{U}$  is orthogonal, also  $\tilde{U}^T Y \sim \mathcal{N}(0, \text{Id}_d)$ . Observe that the distribution of  $U^T Y$  is a marginal distribution of the distribution of  $\tilde{U}^T Y$ . Hence  $U^T Y \sim \mathcal{N}(0, \text{Id}_{d-1})$ . This implies  $\frac{U^T Y}{\|U^T Y\|} \sim \mathcal{U}_{\mathbb{S}^{d-2}} = \frac{1}{\omega_{d-2}} \sigma_{d-2}$ . Using (18) and that  $\varphi_x$  is a linear isometry, we obtain for  $A \in \mathcal{B}(\mathbb{S}_x^{d-2})$  that

$$\begin{aligned} \mathbb{P}\left(\frac{Y - x^T Y x}{\|Y - x^T Y x\|} \in A\right) &= \mathbb{P}\left(\varphi_x\left(\frac{U^T Y}{\|U^T Y\|}\right) \in A\right) = \mathbb{P}\left(\frac{U^T Y}{\|U^T Y\|} \in \varphi_x^{-1}(A)\right) \\ &= \frac{1}{\omega_{d-2}} \sigma_{d-2}(\varphi_x^{-1}(A)) = \frac{1}{\omega_{d-2}} \mu_x(A) = \mathcal{U}_{\mathbb{S}_x^{d-2}}(A). \quad \blacksquare \end{aligned}$$

## Appendix B. Proof of Lemma 1 and Lemma 2

We start with the proof of Lemma 1 that follows by an elementary calculation.

**Proof** (*Proof of Lemma 1.*) For  $x \in \mathbb{S}^{d-1}$ ,  $v \in \mathbb{S}_x^{d-2}$  and  $\theta \in \mathbb{R}$ , using classic trigonometric identities of sine and cosine, we obtain for all  $r \in \mathbb{R}$  that

$$\begin{aligned} \gamma_{T_\theta(x,v)}(r) &= \cos(r)(\cos(\theta)x + \sin(\theta)v) + \sin(r)(\sin(\theta)x - \cos(\theta)v) \\ &= \cos(\theta - r)x + \sin(\theta - r)v = \gamma_{(x,v)}(\theta - r). \end{aligned}$$

This implies  $\gamma_{T_\theta(x,v)}(\theta) = \gamma_{(x,v)}(0) = \cos(0)x + \sin(0)v = x$ . \blacksquare

We turn to the proof of Lemma 2. For convenience we introduce

$$\mathcal{L}(A) := \int_{\mathbb{S}^{d-1}} \int_{\mathbb{S}_x^{d-2}} \mathbb{1}_A(x, v) \mu_x(dv) \sigma_{d-1}(dx), \quad A \in \mathcal{B}(\mathcal{S}\mathbb{S}^{d-1}), \quad (19)$$

for the measure on  $\mathcal{S}\mathbb{S}^{d-1} = \bigcup_{x \in \mathbb{S}^{d-1}} (\{x\} \times \mathbb{S}_x^{d-2})$  that “sews” up the volume measure on the fibers of  $\mathcal{S}\mathbb{S}^{d-1}$  by the volume measures on  $\mathbb{S}^{d-1}$ , and call  $\mathcal{L}$  the *Liouville measure*. We also use the following map.

**Definition 19** *Let  $\theta \in \mathbb{R}$ . The function*

$$\psi_\theta : \mathcal{S}\mathbb{S}^{d-1} \rightarrow \mathcal{S}\mathbb{S}^{d-1}, \quad (x, v) \mapsto (\cos(\theta)x + \sin(\theta)v, -\sin(\theta)x + \cos(\theta)v)$$

*is called the geodesic flow on the sphere.*

To prove Lemma 2 we exploit that we can write  $T_\theta$  as a composition of the geodesic flow and a “sign flip” in the second component. Then Lemma 2 follows by invariance properties of the Liouville measure. Note that when naming  $\mathcal{L}$  and  $\psi_\theta$  we adhere to the terminology of Riemannian geometry.

**Proof** (*Proof of Lemma 2.*) Let  $\theta \in \mathbb{R}$ , and note that the Liouville measure is invariant w.r.t. the geodesic flow, that is,

$$\mathcal{L}(\psi_\theta^{-1}(A)) = \mathcal{L}(A), \quad \forall A \in \mathcal{B}(\mathcal{S}\mathbb{S}^{d-1}),$$

(see e.g., Chavel, 1984, Section V.2). Moreover, define

$$\iota : \mathcal{S}\mathbb{S}^{d-1} \rightarrow \mathcal{S}\mathbb{S}^{d-1}, \quad (x, v) \mapsto (x, -v).$$

Observe that the Liouville measure is invariant under  $\iota$  (see e.g., Paternain, 1999, Lemma 1.34). We can express the map  $T_\theta$  as  $T_\theta = \iota \circ \psi_\theta$ . Therefore the invariance of the Liouville measure under  $\psi_\theta$  and  $\iota$  yields

$$\begin{aligned} \int_{\mathbb{S}\mathbb{S}^{d-1}} F(T_\theta(y)) \mathcal{L}(dy) &= \int_{\mathbb{S}\mathbb{S}^{d-1}} (F \circ \iota \circ \psi_\theta)(y) \mathcal{L}(dy) = \int_{\mathbb{S}\mathbb{S}^{d-1}} (F \circ \iota)(y) \mathcal{L}(dy) \\ &= \int_{\mathbb{S}\mathbb{S}^{d-1}} F(y) \mathcal{L}(dy). \end{aligned} \quad \blacksquare$$

### Appendix C. Proof of Proposition 5

A useful tool for showing reversibility of Markov kernels exhibiting the same structure as the ideal geodesic slice sampling kernel is Lemma 1 by Łatuszyński and Rudolf (2024). It applies to subsets of  $\mathbb{R}^d$  in its original formulation, but can be extended to arbitrary  $\sigma$ -finite measure spaces. For the convenience of the reader we adapt the relevant parts of the aforementioned lemma to our setting.

**Lemma 20** *Let*

$$P(x, A) := \frac{1}{p(x)} \int_0^{p(x)} P_t(x, A \cap L(t)) dt, \quad x \in \mathbb{S}^{d-1}, A \in \mathcal{B}(\mathbb{S}^{d-1}),$$

be a Markov kernel where  $P_t : L(t) \times \mathcal{B}(L(t)) \rightarrow [0, 1]$  for  $t \in (0, \|p\|_\infty)$  are themselves Markov kernels. If  $P_t$  is reversible with respect to  $\mathcal{U}_{L(t)}$  for all  $t \in (0, \|p\|_\infty)$ , then  $P$  is reversible with respect to  $\pi$ .

**Remark 21** *By the fact that  $p$  is lower semicontinuous for any  $t \in (0, \|p\|_\infty)$  we have that  $L(t)$  is open and non-empty. Therefore,  $\sigma_{d-1}(L(t)) \in (0, \infty)$  such that  $\mathcal{U}_{L(t)}$  is well defined.*

We add an auxiliary result w.r.t. the volume of the geodesic level sets under the map  $T_\theta$ .

**Lemma 22** *Let  $x \in \mathbb{S}^{d-1}$ ,  $v \in \mathbb{S}_x^{d-2}$  and  $t \in (0, \|p\|_\infty)$ . Then, for all  $\theta \in \mathbb{R}$  we have  $\lambda(L(T_\theta(x, v), t)) = \lambda(L(x, v, t))$ .*

**Proof** Let  $x \in \mathbb{S}^{d-1}$ ,  $v \in \mathbb{S}_x^{d-2}$  and  $t \in (0, \|p\|_\infty)$ . For  $\theta \in \mathbb{R}$  set

$$w_\theta : [0, 2\pi) \rightarrow [0, 2\pi), \quad r \mapsto (\theta - r) \cdot \mathbb{1}_{(-\infty, \theta]}(r) + (\theta - r + 2\pi) \cdot \mathbb{1}_{(\theta, \infty)}(r).$$

Due to the  $2\pi$ -periodicity of sine and cosine, we have  $L(T_\theta(x, v), t) = w_\theta^{-1}(L(x, v, t))$ . We obtain  $\lambda(L(T_\theta(x, v), t)) = \lambda(w_\theta^{-1}(L(x, v, t))) = \lambda(L(x, v, t))$ , since the Lebesgue measure  $\lambda$  is invariant under  $w_\theta$ .  $\blacksquare$

**Proof** (*Proof of Proposition 5.*) For  $t \in (0, \|p\|_\infty)$  and  $A, B \in \mathcal{B}(\mathbb{S}^{d-1})$  Lemma 2 implies

$$\begin{aligned} &\omega_{d-2} \int_{B \cap L(t)} H_t(x, A) \sigma_{d-1}(dx) \\ &= \int_{B \cap L(t)} \int_{\mathbb{S}_x^{d-2}} \frac{1}{\lambda(L(x, v, t))} \int_{L(x, v, t)} \mathbb{1}_A(\gamma_{(x, v)}(\theta)) d\theta \mu_x(dv) \sigma_{d-1}(dx) \\ &= \int_{[0, 2\pi)} \int_{\mathbb{S}^{d-1}} \int_{\mathbb{S}_x^{d-2}} \frac{\mathbb{1}_{L(T_\theta(x, v), t)}(\theta) \mathbb{1}_{B \cap L(t)}(\gamma_{(x, v)}(\theta)) \mathbb{1}_A(\gamma_{T_\theta(x, v)}(\theta))}{\lambda(L(T_\theta(x, v), t))} \mu_x(dv) \sigma_{d-1}(dx) d\theta. \end{aligned}$$

Then (5), Lemma 1 and Lemma 22 yield

$$\begin{aligned}
 & \omega_{d-2} \int_{B \cap L(t)} H_t(x, A) \sigma_{d-1}(dx) \\
 &= \int_{[0, 2\pi)} \int_{\mathbb{S}^{d-1}} \int_{\mathbb{S}_x^{d-2}} \frac{1}{\lambda(L(x, v, t))} \mathbb{1}_{L(t)}(x) \mathbb{1}_B(\gamma_{(x, v)}(\theta)) \mathbb{1}_{L(x, v, t)}(\theta) \mathbb{1}_A(x) \mu_x(dv) \sigma_{d-1}(dx) d\theta \\
 &= \omega_{d-2} \int_{A \cap L(t)} H_t(x, B) \sigma_{d-1}(dx).
 \end{aligned}$$

Hence,  $H_t$  is reversible w.r.t.  $\mathcal{U}_{L(t)} = \frac{1}{\sigma_{d-1}(L(t))} \sigma_{d-1}|_{L(t)}$ . Lemma 20 then implies that  $H$  is reversible with respect to  $\pi$ .  $\blacksquare$

## Appendix D. Proof of Lemma 11

In this section we prove the integral estimate of Lemma 11. A major part of deriving it consists of handling the measure resulting from exploring the sphere along the great circle passing through a fixed  $x \in \mathbb{S}^{d-1}$ . At first sight, one could think that this measure is  $\sigma_{d-1}$ . Keeping in mind though that, interpreting  $x$  as the “north pole”, the great circle lie much “denser” at the poles than at the equator, it becomes rather clear that  $\sigma_{d-1}$  can only be a lower estimate for the measure obtained by exploring  $\mathbb{S}^{d-1}$  via the great circle through  $x$ .

To prove the desired statement, we make use of an expression for  $\sigma_{d-1}$  in terms of polar coordinates (see Schilling, 2017, Corollary 16.19). Define the polar coordinate transformations

$$\begin{aligned}
 f_{d-1} : (0, \pi)^{d-2} \times (-\pi, \pi) &\rightarrow \mathbb{R}^d \setminus \{(x_1, \dots, x_d)^T \in \mathbb{R}^d \mid x_d = 0, x_{d-1} \leq 0\}, \\
 (\theta_1, \dots, \theta_{d-1}) &\mapsto \begin{pmatrix} \cos(\theta_1) \\ \sin(\theta_1) \cos(\theta_2) \\ \prod_{i=1}^2 \sin(\theta_i) \cos(\theta_3) \\ \vdots \\ \prod_{i=1}^{d-2} \sin(\theta_i) \cos(\theta_{d-1}) \\ \prod_{i=1}^{d-1} \sin(\theta_i) \end{pmatrix},
 \end{aligned}$$

and the absolute value of their Jacobians

$$J_{d-1}(\theta_1, \dots, \theta_{d-1}) = \sin^{d-2}(\theta_1) \sin^{d-3}(\theta_2) \cdot \dots \cdot \sin(\theta_{d-2}).$$

Then for all  $A \in \mathcal{B}(\mathbb{S}^{d-1})$  we have

$$\sigma_{d-1}(A) = \int_0^\pi \dots \int_0^\pi \int_{-\pi}^\pi \mathbb{1}_A(f_{d-1}(\theta_1, \dots, \theta_{d-1})) J_{d-1}(\theta_1, \dots, \theta_{d-1}) d\theta_{d-1} \dots d\theta_1. \quad (20)$$

**Proof** (*Proof of Lemma 11.*) Recall that  $\mu_x = \varphi_x(\sigma_{d-2})$  where  $\varphi_x$  is defined in (17). This allows us to shift from  $\mathbb{S}_x^{d-2}$  to  $\mathbb{S}^{d-2}$ , where we may use the previous explicit expression in

polar coordinates. That is, applying (20) to  $\sigma_{d-2}$  we get

$$\begin{aligned} \int_0^\pi \int_{\mathbb{S}_x^{d-2}} \mathbb{1}_A(\gamma_{(x,v)}(\theta)) \mu_x(dv) d\theta &= \int_0^\pi \int_{\mathbb{S}^{d-2}} \mathbb{1}_A(\gamma_{(x,\varphi_x(y))}(\theta)) \sigma_{d-2}(dy) d\theta \\ &= \int_0^\pi \int_0^\pi \cdots \int_0^\pi \int_{-\pi}^\pi \mathbb{1}_A(\gamma_{(x,\varphi_x(f_{d-2}(\theta_1, \dots, \theta_{d-2})))}(\theta)) J_{d-2}(\theta_1, \dots, \theta_{d-2}) d\theta_{d-2} \cdots d\theta_1 d\theta. \end{aligned}$$

Now, we can use the outer integral (corresponding to travelling along the great circles) to add a dimension in the explicit polar coordinate representation of the volume measure on the sphere at the cost of introducing a correction term. To this end, extend the map  $\varphi_x$  to

$$\tilde{\varphi}_x : \mathbb{S}^{d-1} \rightarrow \mathbb{S}^{d-1}, \quad (y_1, \dots, y_d) \mapsto y_1 x + \sum_{i=1}^{d-1} y_{i+1} e_i^{(x)}.$$

Observe that this reparametrization of  $\mathbb{S}^{d-1}$  is compatible with the geodesic structure of the sphere, because it respects the basis of  $\mathbb{S}_x^{d-2}$  chosen by the map  $\varphi_x$ . More precisely,

$$\gamma_{(x,\varphi_x(f_{d-2}(\theta_1, \dots, \theta_{d-2})))}(\theta) = \tilde{\varphi}_x(f_{d-1}(\theta, \theta_1, \dots, \theta_{d-2})).$$

Furthermore, defining

$$g : \mathbb{R}^d \setminus \{(y_1, \dots, y_d) \in \mathbb{R}^d \mid |y_1| > 1\} \rightarrow \mathbb{R}_+, \quad (y_1, \dots, y_d) \mapsto \frac{1}{\sin^{d-2}(\arccos(y_1))},$$

we have

$$J_{d-2}(\theta_1, \dots, \theta_{d-2}) = g(f_{d-1}(\theta, \theta_1, \dots, \theta_{d-2})) J_{d-1}(\theta, \theta_1, \dots, \theta_{d-2}).$$

Therefore

$$\begin{aligned} \int_0^\pi \int_{\mathbb{S}_x^{d-2}} \mathbb{1}_A(\gamma_{(x,v)}(\theta)) \mu_x(dv) d\theta &= \int_0^\pi \int_0^\pi \cdots \int_0^\pi \int_{-\pi}^\pi \mathbb{1}_A(\tilde{\varphi}_x(f_{d-1}(\theta, \theta_1, \dots, \theta_{d-2}))) g(f_{d-1}(\theta, \theta_1, \dots, \theta_{d-2})) \\ &\quad \cdot J_{d-1}(\theta, \theta_1, \dots, \theta_{d-2}) d\theta_{d-2} \cdots d\theta_1 d\theta. \end{aligned}$$

Applying (20) for  $\sigma_{d-1}$  we obtain

$$\int_0^\pi \int_{\mathbb{S}_x^{d-2}} \mathbb{1}_A(\gamma_{(x,v)}(\theta)) \mu_x(dv) d\theta = \int_{\mathbb{S}^{d-1}} \mathbb{1}_A(\tilde{\varphi}_x(y)) g(y) \sigma_{d-1}(dy).$$

Observe that  $0 \leq \sin^{d-2} \circ \arccos \leq 1$ , such that  $g \geq 1$ . Moreover,  $\sigma_{d-1}$  is invariant under the orthogonal map  $\tilde{\varphi}_x$ . Hence,

$$\int_0^\pi \int_{\mathbb{S}_x^{d-2}} \mathbb{1}_A(\gamma_{(x,v)}(\theta)) \mu_x(dv) d\theta \geq \int_{\mathbb{S}^{d-1}} \mathbb{1}_A(\tilde{\varphi}_x(y)) \sigma_{d-1}(dy) = \sigma_{d-1}(A).$$

Finally, take into account that  $\mathcal{U}_{\mathbb{S}^{d-1}} = \frac{1}{\omega_{d-1}} \sigma_{d-1}$ ,  $\mathcal{U}_{\mathbb{S}_x^{d-2}} = \frac{1}{\omega_{d-2}} \mu_x$  and  $\frac{\omega_{d-1}}{\omega_{d-2}} \geq \frac{\sqrt{2\pi}}{\sqrt{d-1}}$ , cf. (Mathé and Novak, 2007, Lemma 6) as well as the formulas for  $\omega_{d-1}, \omega_{d-2}$  in terms of the Gamma function.  $\blacksquare$

## Appendix E. Proof of Proposition 15.

Hasenpflug et al. (2024) provide a formal description, with a reversibility result, of the shrinkage scheme that we use in the proof of Proposition 15. For convenience of the reader we restate it and state the corresponding reversibility result.

To this end we call a set  $S \in \mathcal{B}([0, 2\pi])$  *open on the circle* if for all  $\theta \in S$  there exists  $\varepsilon > 0$  such that  $\{a \bmod 2\pi \mid |a - \theta| < \varepsilon, a \in \mathbb{R}\} \subseteq S$ . Moreover, for  $a, b \in [0, 2\pi)$  define generalized intervals

$$I(a, b) := \begin{cases} [0, b) \cup [a, 2\pi), & a > b \\ [a, b), & a < b \\ [0, 2\pi), & a = b, \end{cases} \quad \bar{I}(a, b) := \begin{cases} [0, b) \cup [a, 2\pi), & a > b \\ [a, b), & a < b \\ \emptyset, & a = b, \end{cases}$$

that appear in Algorithm 6, which is called as  $\overline{\text{shrink}}(\theta, S)$  for  $S \in \mathcal{B}([0, 2\pi])$  being open on the circle and  $\theta \in S$ .

---

**Algorithm 6** Algorithm 2.2 from Hasenpflug et al. (2024) with input  $S \in \mathcal{B}([0, 2\pi])$  and  $\theta \in S$ , called by  $\overline{\text{shrink}}(\theta, S)$ .

---

**input:** current state  $\theta \in S$

**output:** step-size  $\alpha$

- 1: Set  $i := 1$  and draw  $\Lambda_i \sim \mathcal{U}_{(0, 2\pi)}$ , call the result  $a_i$ .
  - 2: Set  $a_i^{\min} := a_i$  and  $a_i^{\max} := a_i$ .
  - 3: **while**  $a_i \notin S$  **do**
  - 4:   **if**  $a_i \in \bar{I}(a_i^{\min}, \theta)$  **then**
  - 5:     Set  $a_{i+1}^{\min} := a_i$  and  $a_{i+1}^{\max} := a_i^{\max}$ .
  - 6:   **else**
  - 7:     Set  $a_{i+1}^{\min} = a_i^{\min}$  and  $a_{i+1}^{\max} = a_i$ .
  - 8:   **end if**
  - 9:   Draw  $\Lambda_{i+1} \sim \mathcal{U}_{I(a_{i+1}^{\min}, a_{i+1}^{\max})}$ , call the result  $a_{i+1}$ .
  - 10:   Set  $i := i + 1$ .
  - 11: **end while**
  - 12: Return  $\alpha := a_i$ .
- 

For a given set  $S \in \mathcal{B}([0, 2\pi])$  that is open on the circle the transition kernel defined by Algorithm 6 is denoted by

$$\bar{Q}_S : S \times \mathcal{B}(S) \rightarrow [0, 1], \quad (21)$$

that is,

$$\bar{Q}_S(\theta, A) = \mathbb{P}(\overline{\text{shrink}}(\theta, S) \in A), \quad \forall \theta \in [0, 2\pi), A \in \mathcal{B}([0, 2\pi)).$$

Similarly as in Hasenpflug et al. (2024) observe that for  $S = L(x, v, t)$  with  $x \in \mathbb{S}^{d-1}$ ,  $v \in \mathbb{S}_x^{d-2}$  and  $t \in (0, p(x))$ , holds

$$Q_{x,v,t}(\cdot) = \mathbb{P}(\text{shrink}(x, v, t) \in \cdot) = \mathbb{P}(\overline{\text{shrink}}(0, L(x, v, t)) \in \cdot) = \bar{Q}_{L(x,v,t)}(0, \cdot), \quad (22)$$

where the distribution  $Q_{x,v,t}$  is provided in Definition 12. We state two useful properties of the kernel of the shrinkage procedure  $\bar{Q}_S$  that are proven by Hasenpflug et al. (2024).

**Lemma 23 (Hasenpflug et al., 2024, Theorem 2.9)** *Let  $S \in \mathcal{B}([0, 2\pi])$  be non-empty and open on the circle. Then,  $\bar{Q}_S$  defined in (21) is reversible w.r.t.  $\mathcal{U}_S$ .*

**Lemma 24 (Hasenpflug et al., 2024, Lemma 2.10)** *Let  $S \in \mathcal{B}([0, 2\pi])$  be non-empty and open on the circle,  $\theta \in [0, 2\pi)$ , and define  $g_\theta : [0, 2\pi) \rightarrow [0, 2\pi)$  as  $a \mapsto (\theta - a) \bmod 2\pi$ . Then*

$$\bar{Q}_{g_\theta^{-1}(S)}(g_\theta^{-1}(\alpha), g_\theta^{-1}(A)) = \bar{Q}_S(\alpha, A), \quad \forall \alpha \in S, A \in \mathcal{B}(S).$$

Intuitively, the map  $g_\theta$  from the previous lemma corresponds to following a line in reverse direction with an offset of  $\theta$ . The lemma tells us if we apply this motion to all inputs of the shrinkage procedure simultaneously, its effects cancel. We formulate the consequences for our setting.

By Lemma 1 and the  $2\pi$ -periodicity of sine and cosine, we have

$$\gamma_{(x,y)}(g_\theta(a)) = \gamma_{T_\theta(x,v)}(a), \quad \forall x \in \mathbb{S}^{d-1}, v \in \mathbb{S}_x^{d-2}, \theta, a \in [0, 2\pi).$$

This implies for all  $x \in \mathbb{S}^{d-1}, v \in \mathbb{S}_x^{d-2}, \theta \in [0, 2\pi), t \in (0, p(x))$  and  $B \in \mathcal{B}(\mathbb{S}^{d-1})$  that

$$g_\theta^{-1}(L(x, v, t)) = L(T_\theta(x, v), t) \quad \text{and} \quad g_\theta^{-1}\left(\gamma_{(x,v)}^{-1}(B)\right) = \gamma_{T_\theta(x,v)}^{-1}(B).$$

Hence, by applying Lemma 24 for  $A = \gamma_{(x,v)}^{-1}(B)$ ,  $\alpha = \theta$  and  $S = L(x, v, t)$ , we obtain

$$\bar{Q}_{L(T_\theta(x,v),t)}\left(0, \gamma_{T_\theta(x,v)}^{-1}(B)\right) = \bar{Q}_{g_\theta^{-1}(L(x,v,t))}\left(0, g_\theta^{-1}\left(\gamma_{(x,v)}^{-1}(B)\right)\right) = \bar{Q}_{L(x,v,t)}(\theta, \gamma_{(x,v)}^{-1}(B)). \quad (23)$$

To prove Proposition 15 we show reversibility of  $\tilde{H}_t$  w.r.t.  $\mathcal{U}_{L(t)}$  for all  $t \in (0, \|p\|_\infty)$  and then conclude the assertion by Lemma 20. To achieve this, we use the invariance of the Liouville measure under  $T_\theta$  (which corresponds to ‘‘a forward move with a U-turn’’). This boils down to starting the shrinkage procedure at a random point on the geodesic level set.

**Proof (Proof of Proposition 15.)** Let  $t \in (0, \|p\|_\infty)$  and  $A, B \in \mathcal{B}(\mathbb{S}^{d-1})$ . Due to the lower semicontinuity of  $p$ , the level set  $L(t)$  is open. Thus,  $L(x, v, t)$  is non-empty and open on the circle for all  $x \in L(t)$  with  $v \in \mathbb{S}_x^{d-2}$ . Moreover, Lemma 3 implies that  $\lambda(L(x, v, t)) > 0$  for all  $x \in L(t)$  and  $v \in \mathbb{S}_x^{d-2}$ . Hence, we have, exploiting (22), that

$$\begin{aligned} \omega_{d-2} \int_{B \cap L(t)} \tilde{H}_t(x, A) \sigma_{d-1}(dx) &= \int_{B \cap L(t)} \int_{\mathbb{S}_x^{d-2}} \bar{Q}_{L(x,v,t)}(0, \gamma_{(x,v)}^{-1}(A)) \mu_x(dv) \sigma_{d-1}(dx) \\ &= \int_{[0, 2\pi)} \int_{B \cap L(t)} \int_{\mathbb{S}_x^{d-2}} \frac{\mathbb{1}_{L(x,v,t)}(\theta)}{\lambda(L(x, v, t))} \bar{Q}_{L(x,v,t)}(0, \gamma_{(x,v)}^{-1}(A)) \mu_x(dv) \sigma_{d-1}(dx) d\theta. \end{aligned}$$

Then, Lemma 2 yields

$$\begin{aligned} \omega_{d-2} \int_{B \cap L(t)} \tilde{H}_t(x, A) \sigma_{d-1}(dx) &= \int_{[0, 2\pi)} \int_{\mathbb{S}^{d-1}} \int_{\mathbb{S}_x^{d-2}} \mathbb{1}_{B \cap L(t)}(\gamma_{(x,v)}(\theta)) \frac{\mathbb{1}_{L(T_\theta(x,v),t)}(\theta)}{\lambda(L(T_\theta(x, v), t))} \\ &\quad \times \bar{Q}_{L(T_\theta(x,v),t)}(0, \gamma_{T_\theta(x,v)}^{-1}(A)) \mu_x(dv) \sigma_{d-1}(dx) d\theta. \end{aligned}$$

Using (23), (5), Lemma 1 and Lemma 22, we obtain

$$\begin{aligned}
 & \omega_{d-2} \int_{B \cap L(t)} \tilde{H}_t(x, A) \sigma_{d-1}(dx) \\
 &= \int_{[0, 2\pi)} \int_{\mathbb{S}^{d-1}} \int_{\mathbb{S}_x^{d-2}} \mathbb{1}_B(\gamma_{(x,v)}(\theta)) \frac{\mathbb{1}_{L(x,v,t)}(\theta) \mathbb{1}_{L(t)}(x)}{\lambda(L(x,v,t))} \bar{Q}_{L(x,v,t)}(\theta, \gamma_{(x,v)}^{-1}(A)) \mu_x(dv) \sigma_{d-1}(dx) d\theta \\
 &= \int_{L(t)} \int_{\mathbb{S}_x^{d-1}} \frac{1}{\lambda(L(x,v,t))} \int_{\gamma_{(x,v)}^{-1}(B) \cap L(x,v,t)} \bar{Q}_{L(x,v,t)}(\theta, \gamma_{(x,v)}^{-1}(A)) d\theta \mu_x(dv) \sigma_{d-1}(dx).
 \end{aligned}$$

As  $L(x, v, t)$  is open on the circle and non-empty for all  $x \in L(t)$  and  $v \in \mathbb{S}_x^{d-2}$ , we may apply Lemma 23 and get

$$\begin{aligned}
 & \omega_{d-2} \int_{B \cap L(t)} \tilde{H}_t(x, A) \sigma_{d-1}(dx) \\
 &= \int_{L(t)} \int_{\mathbb{S}_x^{d-1}} \frac{1}{\lambda(L(x,v,t))} \int_{\gamma_{(x,v)}^{-1}(A) \cap L(x,v,t)} \bar{Q}_{L(x,v,t)}(\theta, \gamma_{(x,v)}^{-1}(B)) d\theta \mu_x(dv) \sigma_{d-1}(dx).
 \end{aligned}$$

Performing the same arguments in reversed order, we get

$$\omega_{d-2} \int_{B \cap L(t)} \tilde{H}_t(x, A) \sigma_{d-1}(dx) = \omega_{d-2} \int_{A \cap L(t)} \tilde{H}_t(x, B) \sigma_{d-1}(dx).$$

Thus, by Lemma 20, we obtain reversibility of  $\tilde{H}$  with respect to  $\pi$ . ■

## Appendix F. Random-walk Metropolis-Hastings on the Sphere.

The random-walk Metropolis-Hastings (RWMH) algorithm uses an isotropic Gaussian proposal kernel. As suggested by Lie et al. (2023), for current state  $x \in \mathbb{S}^{d-1}$  we choose an auxiliary point  $\sqrt{r}x$  in the ambient space  $\mathbb{R}^d$  by generating a radius  $\sqrt{r}$ , with  $r$  being a realization of  $R \sim \text{Gamma}(d/2, 1/2)$ . Then, given  $\sqrt{r}x$  we sample a realization  $y$  from  $Y \sim \text{Normal}(\sqrt{r}x, \varepsilon^2 \text{Id}_d)$ , where  $\varepsilon$  is the step-size of the random walk. Since this  $y$  does not yet lie on the sphere, we radially project and propose  $y/\|y\|$ , which finally is accepted or rejected using the usual acceptance ratio. In Algorithm 7 we provide the corresponding pseudocode.

## Appendix G. Hamiltonian Monte Carlo on the Sphere.

Since RWMH suffers from diffusive behavior, we also test spherical Hamiltonian Monte Carlo (HMC) suggested by Lan et al. (2014) as an alternative MCMC approach. In spherical HMC, the sample space is first augmented by *momenta* or *velocities*  $v \in \mathbb{R}^d$  that are in the tangent space  $E_x$  to  $\mathbb{S}^{d-1}$  at the current sample  $x$ . The momenta follow a standard Normal distribution, and the Markov chain is generated in the space  $\{(x, v) \mid x \in \mathbb{S}^{d-1}, v \in E_x\}$ . Diffusive behavior is suppressed by the special type of proposal step that solves Hamilton's equations of motion by using a leapfrog integrator (Neal, 2011). During leapfrog integration, the gradient of the log probability  $\nabla \log p(x)$  guides the Markov chain, thereby reaching nearby modes in much shorter time than RWMH. The spherical HMC algorithm is detailed



---

**Algorithm 7** Reprojected RWMH on  $\mathbb{S}^{d-1}$  for step-size  $\varepsilon > 0$ .

---

**input:** current state  $x \in \mathbb{S}^{d-1}$

**output:** next state  $x'$

- 1: Draw  $R \sim \text{Gamma}(d/2, 1/2)$ , call the result  $r$ .
  - 2: Draw  $Y \sim \text{Normal}(\sqrt{r}x, \varepsilon^2 \text{Id}_d)$ , call the result  $y$ .
  - 3: Set  $z = y/\|y\|$ .
  - 4: Draw  $U \sim \mathcal{U}(0, 1)$ , call the result  $u$ .
  - 5: **if**  $u \leq \min\{1, p(z)/p(x)\}$  **then**
  - 6:      $x' = z$
  - 7: **else**
  - 8:      $x' = x$
  - 9: **end if**
- 

in Algorithm 8. In contrast to standard HMC, spherical HMC involves a rotation of the positions and momenta during leapfrog integration where the rotation matrix is a Givens rotation  $G(v/\|v\|, x, \theta)$  in the plane spanned by the momenta  $v$  and the positions  $x$  (see lines 8–10 in Algorithm 8 and Equation 4). In addition to the step-size parameter  $\varepsilon > 0$ , we also need to choose the number of leapfrog steps  $T \in \mathbb{N}$ . In our experiments, we always set  $T = 10$ .

## Appendix H. Step-size Tuning for RWMH and HMC

Both RWMH and spherical HMC involve a step-size parameter  $\varepsilon$ . Because a good choice of  $\varepsilon$  depends on the particular shape of our target distribution  $p(x)$ , we first find  $\varepsilon$  automatically during a burn-in phase. During burn-in, we increase  $\varepsilon$  by a factor 1.02, if the proposal (based on the current value of  $\varepsilon$ ) is accepted. We decrease  $\varepsilon$  by a factor 0.98 if the proposed state is rejected. After a burn-in phase, the value of  $\varepsilon$  is kept fixed.

## Appendix I. Tests on 50-dimensional Bingham Distribution.

Tests for the 50-dimensional Bingham distribution with a concentration parameter  $\kappa_{50} = 300$ .

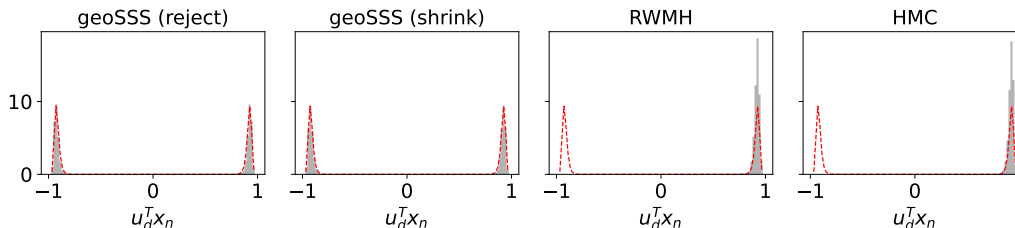


Figure A1: Histograms of approximate Bingham samples ( $d = 50, \kappa_d = 300$ ) projected on the first mode obtained with each MCMC method are shown in grey. The red dashed line indicates the baseline obtained with the acceptance/rejection sampler of Kent et al. (2018).

---

**Algorithm 8** Hamiltonian Monte Carlo on  $\mathbb{S}^{d-1}$  for step-size  $\varepsilon > 0$  and number of integration steps  $T$ .

---

**input:** current state  $x \in \mathbb{S}^{d-1}$

**output:** next state  $x'$

- 1: Draw  $V \sim \text{Normal}(0, \text{Id}_d)$ , call the result  $v$ .
  - 2: Set  $v_1 = (\text{Id}_d - xx^T)v$ ,  $x_1 = x$  and  $t = 1$ .
  - 3: **while**  $t \leq T$  **do**
  - 4:   Set  $v_{t+1/2} = v_t + \frac{\varepsilon}{2} (\text{Id}_d - x_t x_t^T) \nabla \log p(x_t)$ .
  - 5:   Set  $R = G(v_{t+1/2}/\|v_{t+1/2}\|, x_t, \varepsilon \|v_{t+1/2}\|)$ .
  - 6:   Set  $x_{t+1} = R x_t$ .
  - 7:   Set  $v_{t+1} = R v_{t+1/2} + \frac{\varepsilon}{2} (\text{Id}_d - x_{t+1} x_{t+1}^T) \nabla \log p(x_{t+1})$ .
  - 8:   Set  $t := t + 1$ .
  - 9: **end while**
  - 10: Draw  $U \sim \mathcal{U}(0, 1)$ , call the result  $u$ .
  - 11: **if**  $u < \min \{1, \exp(\|v_1\|^2/2 - \|v_{T+1}\|^2/2) p(x_{T+1})/p(x)\}$  **then**
  - 12:   Set  $x' = x_{T+1}$ .
  - 13: **else**
  - 14:   Set  $x' = x$ .
  - 15: **end if**
- 

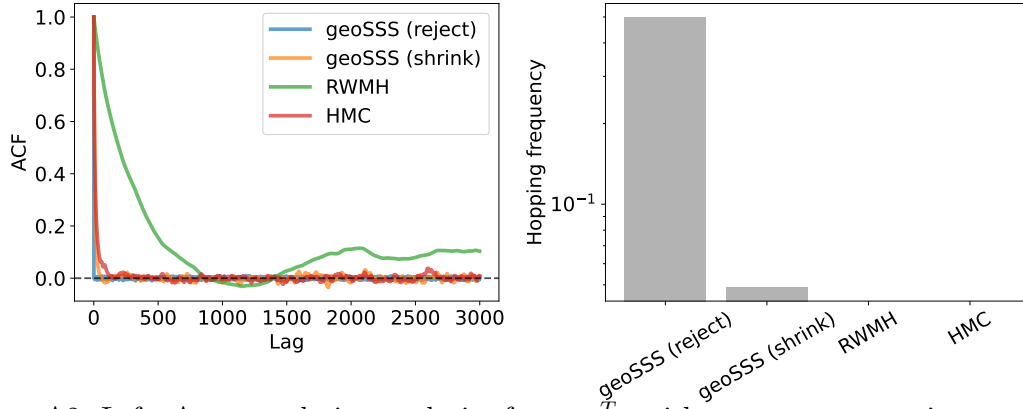


Figure A2: Left: Autocorrelation analysis of  $x \mapsto u_d^T x$  with respect to approximate samples from a Bingham distribution with  $d = 50$  and  $\kappa_d = 300$ . Right: Estimated hopping frequency between both modes of the Bingham distribution. Note that the hopping frequency is shown on a logarithmic axis.

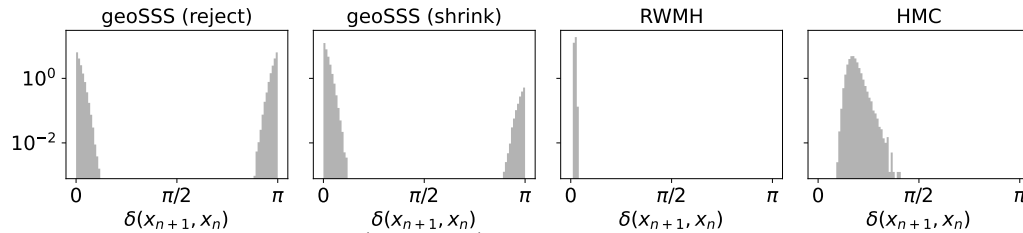


Figure A3: Geodesic distance (log-scale) between successive approximate samples for a Bingham distribution with  $d = 50$  and  $\kappa_d = 300$ .

## Appendix J. Run Times of Numerical Illustrations

We summarize the run times in seconds (s) for all the numerical experiments tested on Intel i7-10510U CPU in Table A1. We nomenclate these experiments for brevity. For the Bingham distribution with  $d = 10$ ,  $\kappa_d = 30$  and  $N = 10^5$  as “Bingham-d10”, for the Bingham distribution with  $d = 50$ ,  $\kappa_d = 300$  and  $N = 10^5$  as “Bingham-d50”, for the mixture of vMF distribution with  $d = 10$ ,  $\kappa = 100$ ,  $K = 5$  and  $N = 10^6$  as “vMF-d10” and for the curve vMF distribution with  $\kappa = 300$  and  $N = 10^5$  as “curved-vMF”.

Numerical Illustrations	MCMC Methods			
	geoSSS (reject)	geoSSS (shrink)	RWMH	HMC
Bingham-d10	13.9 s	8.5 s	3.5 s	28.4 s
Bingham-d50	36.5 s	13.1 s	3.5 s	32.0 s
vMF-d10	2601.6 s	812.9 s	274.4 s	1898.9 s
curved-vMF	926.6 s	419.5 s	151.4 s	1008.1 s

Table A1: Comparison of run times for each MCMC method across different numerical illustrations.

## References

- Claude J. P. Bélisle, H. Edwin Romeijn, and Robert L. Smith. Hit-and-run algorithms for generating multivariate distributions. *Mathematics of Operations Research*, 18(2): 255–266, 1993.
- Alexandros Beskos and Kengo Kamatani. MCMC algorithms for posteriors on matrix spaces. *Journal of Computational and Graphical Statistics*, 31(3):721–738, 2022.
- Simon Byrne and Mark Girolami. Geodesic Monte Carlo on embedded manifolds. *Scandinavian Journal of Statistics*, 40(4):825–845, 2013.
- Isaac Chavel. *Eigenvalues in Riemannian geometry*, volume 115 of *Pure and Applied Mathematics*. Academic Press, Inc., Orlando, FL, 1984.
- Wallace Givens. Computation of plain unitary rotations transforming a general matrix to triangular form. *Journal of the Society for Industrial and Applied Mathematics*, 6(1): 26–50, 1958.
- Navin Goyal and Abhishek Shetty. Sampling and optimization on convex sets in Riemannian manifolds of non-negative curvature. In *Proceedings of the 32nd Conference on Learning Theory*, volume 99, pages 1519–1561. PMLR, 2019.
- Andrew J. Hanson. Rotations for N-dimensional graphics. In Alan W. Paeth, editor, *Graphics Gems V*, pages 55–64. Academic Press, Boston, 1995.

- Mareike Hasenpflug, Viacheslav Telezhnikov, and Daniel Rudolf. Reversibility of elliptical slice sampling revisited. arXiv: 2301.02426v2, 2024. URL <https://arxiv.org/abs/2301.02426>.
- Andrew Holbrook, Shiwei Lan, Jeffrey Streets, and Babak Shahbaba. Nonparametric Fisher geometry with application to density estimation. In *Proceedings of the 36th Conference on Uncertainty in Artificial Intelligence*, volume 124, pages 101–110. PMLR, 2020.
- Marc Kac. Foundations of kinetic theory. In *Proceedings of the 3rd Berkeley Symposium on Mathematical Statistics and Probability*, volume 3, pages 171–197. University of California Press, 1956.
- John T. Kent, Asaad M. Ganeiber, and Kanti V. Mardia. A new unified approach for the simulation of a wide class of directional distributions. *Journal of Computational and Graphical Statistics*, 27(2):291–301, 2018.
- Shiwei Lan, Bo Zhou, and Babak Shahbaba. Spherical Hamiltonian Monte Carlo for constrained target distributions. In *Proceedings of the 31st International Conference on Machine Learning*, volume 32, pages 629–637. PMLR, 2014.
- Krzysztof Łatuszyński and Daniel Rudolf. Convergence of hybrid slice sampling via spectral gap. arXiv: 1409.2709v2, 2024. URL <https://arxiv.org/abs/1409.2709>.
- Yin Tat Lee and Santosh S. Vempala. Convergence rate of Riemannian Hamiltonian Monte Carlo and faster polytope volume computation. In *Proceedings of the 50th Annual ACM SIGACT Symposium on Theory of Computing*, page 1115–1121. Association for Computing Machinery, 2018.
- Han C. Lie, Daniel Rudolf, Björn Sprungk, and Timothy J. Sullivan. Dimension-independent Markov chain Monte Carlo on the sphere. *Scandinavian Journal of Statistics*, 5(4):1818–1858, 2023.
- László Lovász and Santosh Vempala. The geometry of logconcave functions and sampling algorithms. *Random Structures & Algorithms*, 30(3):307–358, 2007.
- Oren Mangoubi and Aaron Smith. Rapid mixing of geodesic walks on manifolds with positive curvature. *The Annals of Applied Probability*, 28(4):2501–2543, 2018.
- Kanti V. Mardia and Peter E. Jupp. *Directional statistics*. John Wiley & Sons, Ltd., Chichester, 2000.
- Augustin Marignier, Jason D. McEwen, Ana M. G. Ferreira, and Thomas D. Kitching. Posterior sampling for inverse imaging problems on the sphere in seismology and cosmology. *RAS Techniques and Instruments*, 2(1):20–32, 2023.
- Peter Mathé and Erich Novak. Simple Monte Carlo and the Metropolis algorithm. *Journal of Complexity*, 23(4):673–696, 2007.
- Sean P. Meyn and Richard L. Tweedie. *Markov chains and stochastic stability*. Cambridge University Press, Cambridge, 2nd edition, 2009.

- James R. Munkres. *Analysis on manifolds*. Addison-Wesley Publishing Company, Redwood City, 1991.
- Iain Murray, Ryan Adams, and David MacKay. Elliptical slice sampling. In *Proceedings of the 13th International Conference on Artificial Intelligence and Statistics*, volume 9, pages 541–548. PMLR, 2010.
- Viacheslav Natarovskii, Daniel Rudolf, and Björn Sprungk. Geometric convergence of elliptical slice sampling. In *Proceedings of the 38th International Conference on Machine Learning*, volume 139, pages 7969–7978. PMLR, 2021a.
- Viacheslav Natarovskii, Daniel Rudolf, and Björn Sprungk. Quantitative spectral gap estimate and Wasserstein contraction of simple slice sampling. *The Annals of Applied Probability*, 31(2):806 – 825, 2021b.
- Radford M. Neal. Slice sampling. *The Annals of Statistics*, 31(3):705–767, 2003.
- Radford M. Neal. MCMC using Hamiltonian dynamics. In Steve Brooks, editor, *Handbook of Markov chain Monte Carlo*, pages 113–162. CRC Press, Boca Raton, FL, 2011.
- Gabriel P. Paternain. *Geodesic flows*, volume 180 of *Progress in Mathematics*. Birkhäuser, Boston, 1999.
- Natesh S. Pillai and Aaron Smith. Kac’s walk on  $n$ -sphere mixes in  $n \log n$  steps. *The Annals of Applied Probability*, 27(1):631–650, 2017.
- Gareth O Roberts and Jeffrey S Rosenthal. Convergence of slice sampler markov chains. *Journal of the Royal Statistical Society Series B: Statistical Methodology*, 61(3):643–660, 1999.
- René L. Schilling. *Measures, integrals and martingales*. Cambridge University Press, Cambridge, 2nd edition, 2017.
- Simon Schwarz, Michael Herrmann, Anja Sturm, and Max Wardetzky. Efficient random walks on Riemannian manifolds. arXiv:2022.00959v2, 2022. URL <https://arxiv.org/abs/2202.00959>.
- Andrew T. A. Wood. Simulation of the von Mises Fisher distribution. *Communications in Statistics - Simulation and Computation*, 23(1):157–164, 1994.
- Jun Yang, Krzysztof Łatuszyński, and Gareth O. Roberts. Stereographic Markov Chain Monte Carlo. arXiv:2205.12112v1, 2022. URL <https://arxiv.org/abs/2205.12112>.